JCI The Journal of Clinical Investigation

Androgen receptor functions as transcriptional repressor of cancer-associated fibroblast activation

Andrea Clocchiatti, Soumitra Ghosh, Maria-Giuseppina Procopio, Luigi Mazzeo, Pino Bordignon, Paola Ostano, Sandro Goruppi, Giulia Bottoni, Atul Katarkar, Mitchell Levesque, Peter Kölblinger, Reinhard Dummer, Victor Neel, Berna C. Özdemir, G. Paolo Dotto

J Clin Invest. 2018. https://doi.org/10.1172/JCI99159.

Research Article **Dermatology** **Oncology**

The aging-associated increase of cancer risk is linked with stromal fibroblast senescence and concomitant cancer-associated fibroblast (CAF) activation. Surprisingly little is known about the role of androgen receptor (AR) signaling in this context. We have found downmodulated AR expression in dermal fibroblasts underlying premalignant skin cancer lesions (actinic keratoses and dysplastic nevi) as well as in CAFs from the 3 major skin cancer types, squamous cell carcinomas (SCCs), basal cell carcinomas, and melanomas. Functionally, decreased AR expression in primary human dermal fibroblasts (HDFs) from multiple individuals induced early steps of CAF activation, and in an orthotopic skin cancer model, AR loss in HDFs enhanced tumorigenicity of SCC and melanoma cells. Forming a complex, AR converged with CSL/RBP-Jκ in transcriptional repression of key CAF effector genes. AR and CSL were positive determinants of each other's expression, with BET inhibitors, which counteract the effects of decreased CSL, restoring AR expression and activity in CAFs. Increased AR expression in these cells overcame the consequences of CSL loss and was by itself sufficient to block the growth and tumor-enhancing effects of CAFs on neighboring cancer cells. As such, the findings establish AR as a target for stroma-focused cancer chemoprevention and treatment.

Androgen receptor functions as transcriptional repressor of cancer-associated fibroblast activation

Andrea Clocchiatti,[1,2] Soumitra Ghosh,[3] Maria-Giuseppina Procopio,[3] Luigi Mazzeo,[3] Pino Bordignon,[3] Paola Ostano,[4] Sandro Goruppi,[1,2] Giulia Bottoni,[1] Atul Katarkar,[3] Mitchell Levesque,[5] Peter Kölblinger,[5,6] Reinhard Dummer,[5] Victor Neel,[7] Berna C. Özdemir,[8,9] and G. Paolo Dotto[1,3,9]

[1]Cutaneous Biology Research Center, Massachusetts General Hospital, Boston, Massachusetts, USA. [2]Department of Dermatology, Harvard Medical School, Boston, Massachusetts, USA. [3]Department of Biochemistry, University of Lausanne, Epalinges, Switzerland. [4]Cancer Genomics Laboratory, Edo and Elvo Tempia Valenta Foundation, Biella, Italy. [5]Department of Dermatology, University Hospital Zürich, Zürich, Switzerland. [6]Department of Dermatology, Paracelsus Medical University, Salzburg, Austria. [7]Department of Dermatology, Massachusetts General Hospital, Boston, Massachusetts, USA. [8]Department of Oncology, Centre Hospitalier Universitaire Vaudois, Lausanne, Switzerland. [9]International Cancer Prevention Institute, Epalinges, Switzerland.

The aging-associated increase of cancer risk is linked with stromal fibroblast senescence and concomitant cancer-associated fibroblast (CAF) activation. Surprisingly little is known about the role of androgen receptor (AR) signaling in this context. We have found downmodulated AR expression in dermal fibroblasts underlying premalignant skin cancer lesions (actinic keratoses and dysplastic nevi) as well as in CAFs from the 3 major skin cancer types, squamous cell carcinomas (SCCs), basal cell carcinomas, and melanomas. Functionally, decreased AR expression in primary human dermal fibroblasts (HDFs) from multiple individuals induced early steps of CAF activation, and in an orthotopic skin cancer model, AR loss in HDFs enhanced tumorigenicity of SCC and melanoma cells. Forming a complex, AR converged with CSL/RBP-Jκ in transcriptional repression of key CAF effector genes. AR and CSL were positive determinants of each other's expression, with BET inhibitors, which counteract the effects of decreased CSL, restoring AR expression and activity in CAFs. Increased AR expression in these cells overcame the consequences of CSL loss and was by itself sufficient to block the growth and tumor-enhancing effects of CAFs on neighboring cancer cells. As such, the findings establish AR as a target for stroma-focused cancer chemoprevention and treatment.

Introduction

The aging-associated increase of many cancer types has been linked with stromal fibroblast senescence and concomitant production of diffusible growth factors, cytokines, and extracellular matrix/remodeling proteins (1) that are similarly induced in cancer-associated fibroblasts (CAFs) (2). However, fully established CAFs show no signs of senescence and are often characterized by increased cell proliferation (3, 4), consistent with a multistep process of CAF activation associated with cancer/stromal cell expansion (5).

Alterations of key regulators of transcription and chromatin organization involved in early steps of CAF activation include downmodulation of CSL/RBP-Jκ (subsequently called CSL), the key effector of Notch signaling endowed with intrinsic transcriptional-repressive function and overall determinant of chromatin configuration (5, 6). CSL functions as a direct negative regulator of many CAF effector genes and at the same time binds to p53, suppressing its activity (5). As a consequence, decreased CSL levels in stromal fibroblasts result in the concomitant induction of CAF effector genes and p53-dependent cellular senescence, with decreased p53 expression and activity occurring as a second step leading to full CAF activation (5).

The impact of hormonal signaling on CAF activation has been scarcely studied. Among hormones, androgens play an important role in both males and females as determinants of systemic functions such as metabolism and immune system (7, 8). In addition, they have a significant impact on tissue processes such as angiogenesis (9), muscle strength, wound healing, and brain activity (10–12). The role of androgens in prostate cancer is well documented (13), and there is emerging evidence that they are also implicated in female tumors, specifically breast cancer (14).

The androgen receptor (AR) has highly context-dependent functions (15). Surprisingly few studies have focused on its role in CAFs, so far limited to prostate cancer with apparently conflicting conclusions (16–21). In a mouse model, loss of stromal AR was reported to limit prostate cancer lesions, while, in human tumors, lower stromal AR expression was associated with a lower degree of cancer cell differentiation and poor prognosis (18).

Like AR, the biological functions of Notch/CSL signaling are highly context dependent (22). So far, only an indirect interplay between AR and Notch signaling has been reported in cellular systems unrelated to CAF activation (23, 24). Here we show that, in dermal fibroblasts, AR and CSL physically converge on negative control of key senescence and CAF effector genes. These findings are of functional and clinical significance, as stromal AR expression is coordinately downmodulated with CSL at premalignant stages of cancer development (actinic keratoses, dysplastic nevi), and, in an orthotopic model, decreased AR expression in dermal fibroblasts promotes tumorigenicity of both skin squamous cell

Authorship note: AC and SG contributed equally to this work.
Conflict of interest: The authors have declared that no conflict of interest exists.

Submitted: December 11, 2017; **Accepted:** September 26, 2018.
Reference information: *J Clin Invest*. https://doi.org/10.1172/JCI99159.

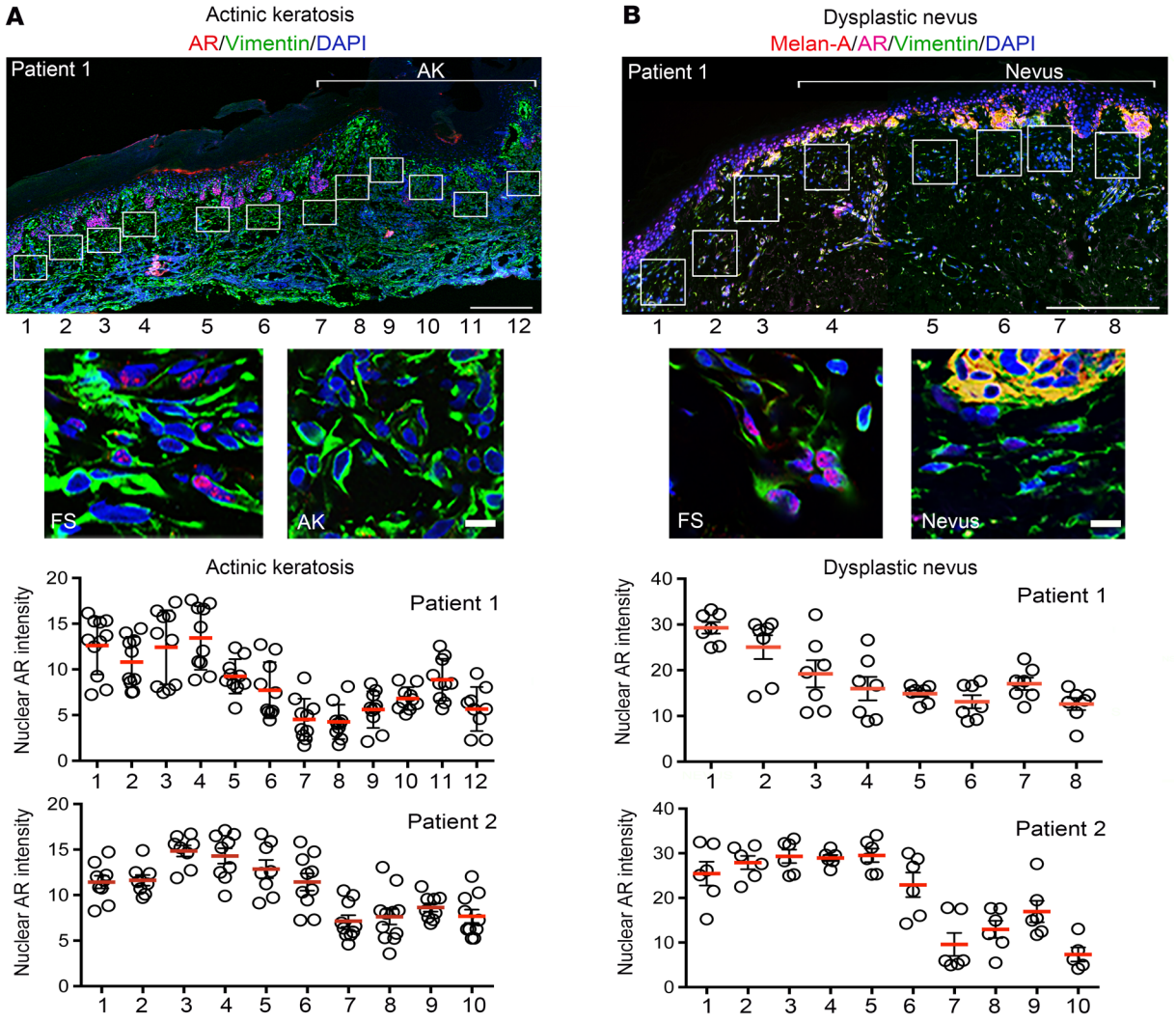

Figure 1. Stromal AR levels are reduced in skin cancer fields. (**A**) Top panels: Double immunofluorescence (IF) analysis of topographically delimited stromal areas (numbered boxes) at various distances from the skin actinic keratosis (AK) lesion from patient 1, with anti-AR (red) and anti-vimentin (green) antibodies. Scale bar: 200 μm. Representative high-magnification IF images used for quantification of AR fluorescence signal in vimentin-positive fibroblasts cells. Scale bar: 20 μm. Bottom panels: Quantification of AR fluorescence signal in vimentin-positive cells within each delimited area from 2 different patients. Values for each individual cell are indicated with mean ± SD. Less than 5% of cells double-stained for vimentin and the CD68 macrophage marker in parallel sections (data not shown). The H&E staining and additional IF images are shown in Supplemental Figure 1A. (**B**) Top panels: Triple-IF analysis of topographically delimited stromal areas (numbered boxes) at various distances from dysplastic nevus lesion from patient 1, with anti–melan-A (red), anti-AR (magenta), and anti-vimentin (green) antibodies. Scale bar: 200 μm. Representative high-magnification IF images used for quantification of AR fluorescence signal in fibroblasts (vimentin-positive and melan-A–negative cells). Scale bar: 20 μm. Bottom panels: Quantification of AR fluorescence signal in the fibroblasts within each delimited area from 2 different patients. Values for each individual cell are indicated with mean ± SD. The immunohistochemical staining and additional IF images are shown in Supplemental Figure 1B.

carcinoma and melanoma cells. Conversely, increased AR expression in CAFs overcomes the consequences of CSL loss and suppresses the growth/tumor-promoting effects that these cells have on neighboring cancer cells. As such, AR is a novel potential target for stroma-focused cancer chemoprevention and treatment.

Results

Decreased AR expression triggers early steps of CAF activation. The skin provides a benchmark for studies on the interplay between stromal changes and early steps of cancer development. The role of AR signaling in this context is largely unknown. Actinic keratoses (AKs) and dysplastic nevi are precancerous lesions that develop frequently in photo-aged skin (25). To assess possible cancer field effects on stromal AR expression, we examined relatively large excisions of two AK lesions and surrounding flanking skin, quantifying immunofluorescence AR signal intensity in dermal fibroblasts within several topographically delimited areas at various distances from the lesions. As shown in Figure 1A and Supplemental Figure 1A (supplemental material available online with this article; https://doi.org/10.1172/JCI99159DS1), we found consistently decreasing AR levels in dermal fibroblasts underneath the lesions as compared with those further away. A similar approach was adopted for "topographical quantification" of AR levels in stromal fibroblasts underlying 2 dysplastic nevi versus skin fur-

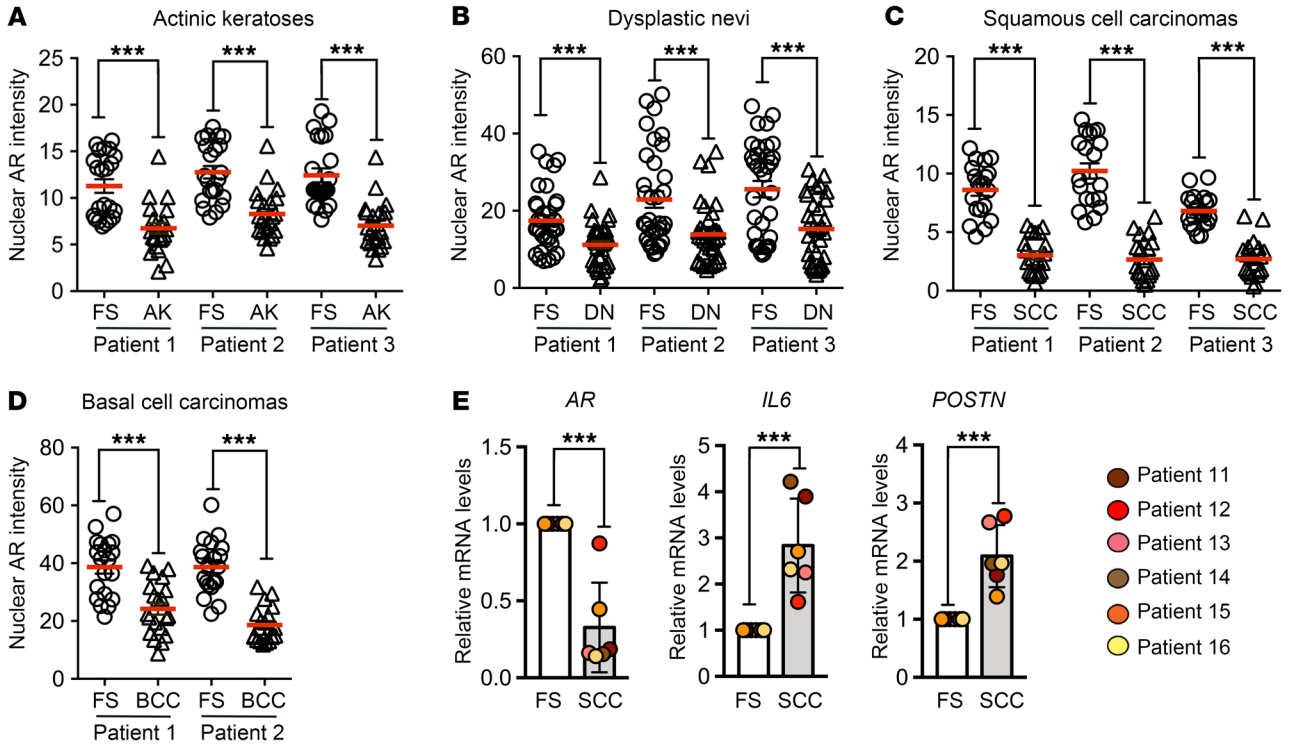

Figure 2. AR expression is downmodulated in stromal fibroblasts of premalignant and malignant skin cancer lesions. (**A**–**D**) Quantification of immunofluorescence analysis of AR signal intensity in vimentin-positive stromal cells underlying actinic keratoses (AK) (**A**), dysplastic nevi (DN) (**B**), squamous cell carcinomas (SCC) (**C**), and basal cell carcinomas (BCC) (**D**) lesions versus flanking skin from multiple patients. For **A** and **B** quantification, the same lesions as in Figure 1A plus those of an additional patient were used for independent quantification of AR signal intensity in lesion-adjacent areas versus flanking skin. For **C** and **D**, stromal cells in SCC- and BCC-adjacent areas versus flanking skin of the same patients excised at the end of the surgical procedure ("dog ears") were used for quantification. Values for each individual cell are indicated with mean ± SD. Representative lower- and higher-magnification images for SCC samples are shown in Supplemental Figure 1C. *n*(vimentin-positive cells per sample) = 25 for **A** and **B**, = 20 for **C** and **D**; ***$P < 0.005$, 2-tailed paired *t* test. (**E**) Fluorescence-guided laser capture microdissection (LCM) of fibroblast (PDGFRα-positive) cells from stroma of SCC lesions versus flanking skin of the same patients was analyzed by RT-qPCR for the indicated genes. Values for each patient are indicated as dots with mean ± SD. *n*(patients) = 6; ***$P < 0.005$, 2-tailed paired *t* test.

ther away. Even in these cases, there was a progressive decrease in AR expression in stromal fibroblasts underlying the lesions versus those in areas further away (Figure 1B and Supplemental Figure 1B). Diminished AR expression in lesion-adjacent fibroblasts was confirmed by analysis of additional AK and dysplastic nevus samples (with a calculation of the statistical significance of the observed differences for all lesions; Figure 2, A and B), as well as of several skin squamous cell carcinomas (SCCs) and basal cell carcinomas (BCCs) relative to cancer-free skin of the same patients excised at the end of the surgical procedure ("dog ears") (Figure 2, C and D, and Supplemental Figure 1C). This analysis could not be extended to invasive melanoma lesions because of overlapping melanocyte and fibroblast markers hampering unequivocal cell identification in tissue sections. Diminished *AR* expression was further confirmed at the mRNA level, by fluorescence-guided laser capture microdissection (LCM) and quantitative reverse transcriptase PCR (RT-qPCR) analysis of SCC-associated stromal fibroblasts, in which CAF markers like *IL6* (interleukin-6) and *POSTN* (periostin) were also increased, versus dog-ears fibroblasts of the same patients (Figure 2E).

Decreased AR level was also observed by immunoblot analysis of multiple strains of human dermal fibroblasts (HDFs) versus CAFs derived from SCCs, BCCs, or melanomas (Figure 3, A–D). Differences in AR expression were also confirmed at the cellular level by immunofluorescence analysis of HDFs versus SCC- and melanoma-derived CAFs (Figure 3, E and F, and Supplemental Figure 2, A and B).

To assess the functional significance of these findings, we evaluated the consequences of *AR* knockdown. Silencing of the gene in several HDF strains resulted in increased expression of α-smooth muscle actin (αSMA), a well-established marker of CAF activation (Supplemental Figure 2C), which was paralleled by induction of a battery of CAF effector genes (Figure 4, A and B). Induction of such genes occurred also upon *AR* gene silencing in lung fibroblasts and in pancreatic stellate cells (Supplemental Figure 3, A and B).

Paralleling the above findings, treatment of several HDF strains with flutamide, a nonsteroidal antagonist that competes with androgens for AR binding and activation (26), also induced expression of CAF effector genes (Figure 4C), which were instead suppressed by treatment with AR agonists such as dihydrotestosterone (DHT) or MK-2866 (SARM) (Figure 4D and Supplemental Figure 3C). No suppressing effects were observed in CAFs even after prolonged DHT treatment for 3 or 7 days, consistent with the low AR levels present in these cells (Supplemental Figure 3, D and E).

Early steps of CAF activation and stromal fibroblast senescence are closely intertwined events. As upon *CSL* knockdown (5), *AR* silencing in multiple HDF strains resulted in reduced proliferation and increased senescence (Figure 5, A and B). This was par-

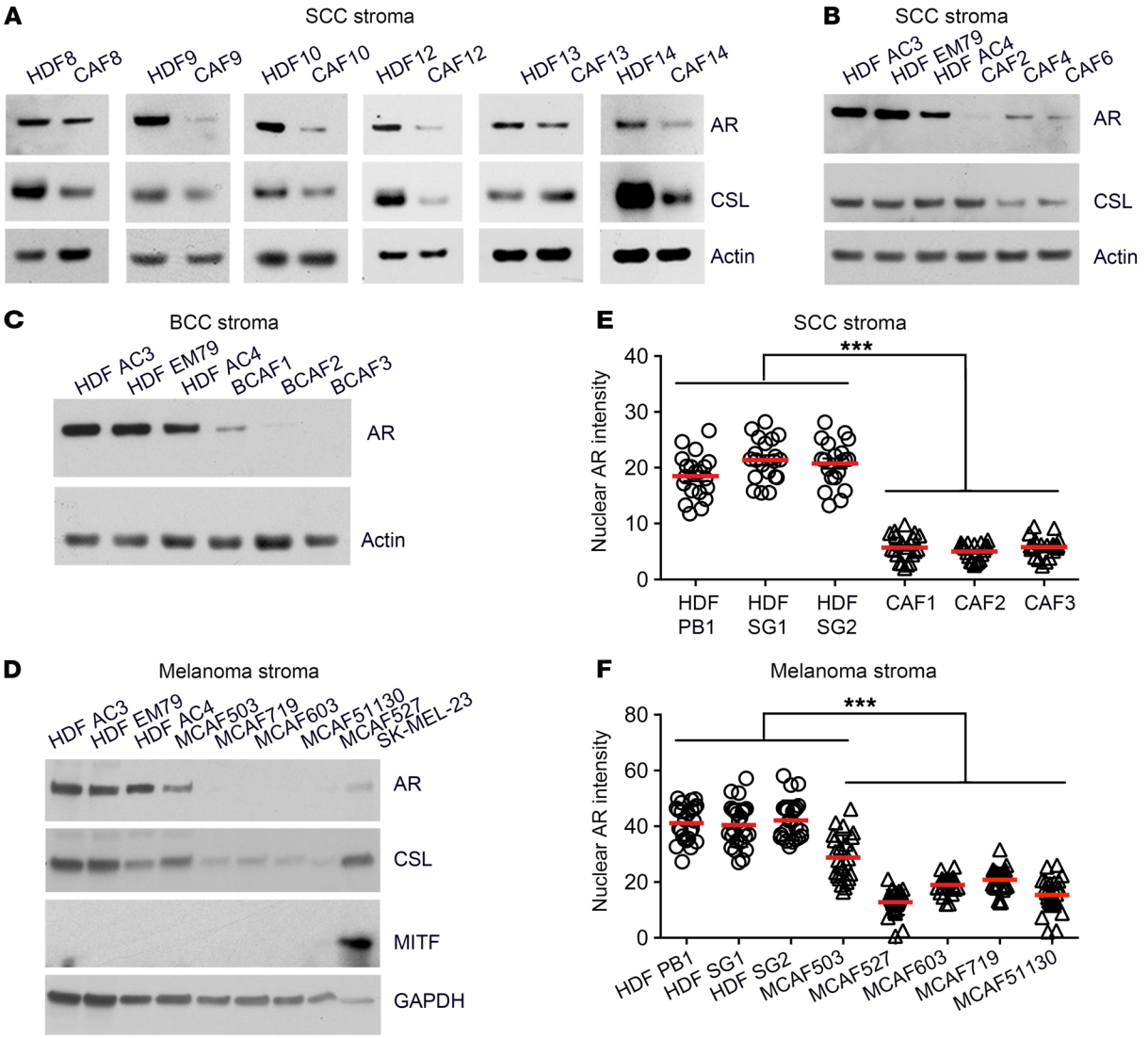

Figure 3. Reduction of AR protein levels is conserved in skin cancer–derived CAFs. (**A** and **B**) Immunoblot analysis of AR and CSL levels in CAF strains derived from multiple skin SCCs and flanking unaffected skin from matched (**A**) or unmatched donors (**B**). The blots were sequentially probed with antibodies against AR, CSL, and β-actin. (**C** and **D**) Immunoblot analysis of AR (**C** and **D**) and CSL (**D**) levels in multiple CAF strains derived from BCC (**C**) and melanoma (**D**) lesions versus a reference set of HDF strains. In the case of melanoma-derived CAFs, samples were run in parallel with an extract of melanoma cells (SK-MEL-23), and the blot was also probed with antibodies against the melanocyte/melanoma marker MITF, to verify that CAF cells were stromal derived (MITF negative). Additionally, DNA sequencing analysis showed oncogenic BRAF or NRAS mutations in the excised melanomas but not in the CAFs derived from these lesions (data not shown). (**E** and **F**) Quantification of immunofluorescence analysis of AR expression in multiple CAF strains derived from skin SCC (**E**) or melanoma (**F**) versus a reference set of HDF strains. Values for each individual cell are indicated with mean ± SD. Twenty cells per strain were counted. Representative images are shown in Supplemental Figure 2A. *n*(HDF strains) = 3, *n*(SCC-derived CAF strains) = 3, *n*(melanoma-derived CAF strains) = 5; ***$P < 0.005$, 2-tailed unpaired *t* test.

alleled by strong suppression of p105-Rb phosphorylation (Ser780 and Ser795), decreased levels of phospho-H3 and PCNA, and downmodulation of the *MKI67* and *c-MYC* proliferation marker genes, while gene expression of cyclin-dependent kinase inhibitors (*CDKN1A* and *CDKN2B*) was induced (Figure 5, C and D).

Together with the above changes, p53 expression was enhanced in HDFs with silenced *AR* at both protein and mRNA levels (Figure 6, A and B). Chromatin immunoprecipitation (ChIP) assays with 3 different HDF strains showed AR binding to 2 consensus-binding sites present in the *TP53* gene promoter and proximal regulatory region, pointing to p53 as a direct negative AR target (Figure 6C). Increased p53 expression by *AR* silencing is of functional significance, as silencing of the gene overcame the growth-suppressing effects of *AR* knockdown (Figure 6D). Molecularly, induction of *CDKN1A* was abrogated by concomitant *AR* and *TP53* silencing, while the upregulation of the *IL6* CAF effector gene occurred to an extent similar to or greater than that seen in controls (Figure 6E), consistent with previous findings that p53 functions as a transcriptional repressor of CAF effector genes (5, 27).

Thus, downmodulation of AR expression or activity is sufficient to trigger early steps of CAF activation, with concomitant induction of CAF effector genes and p53-dependent cellular senescence.

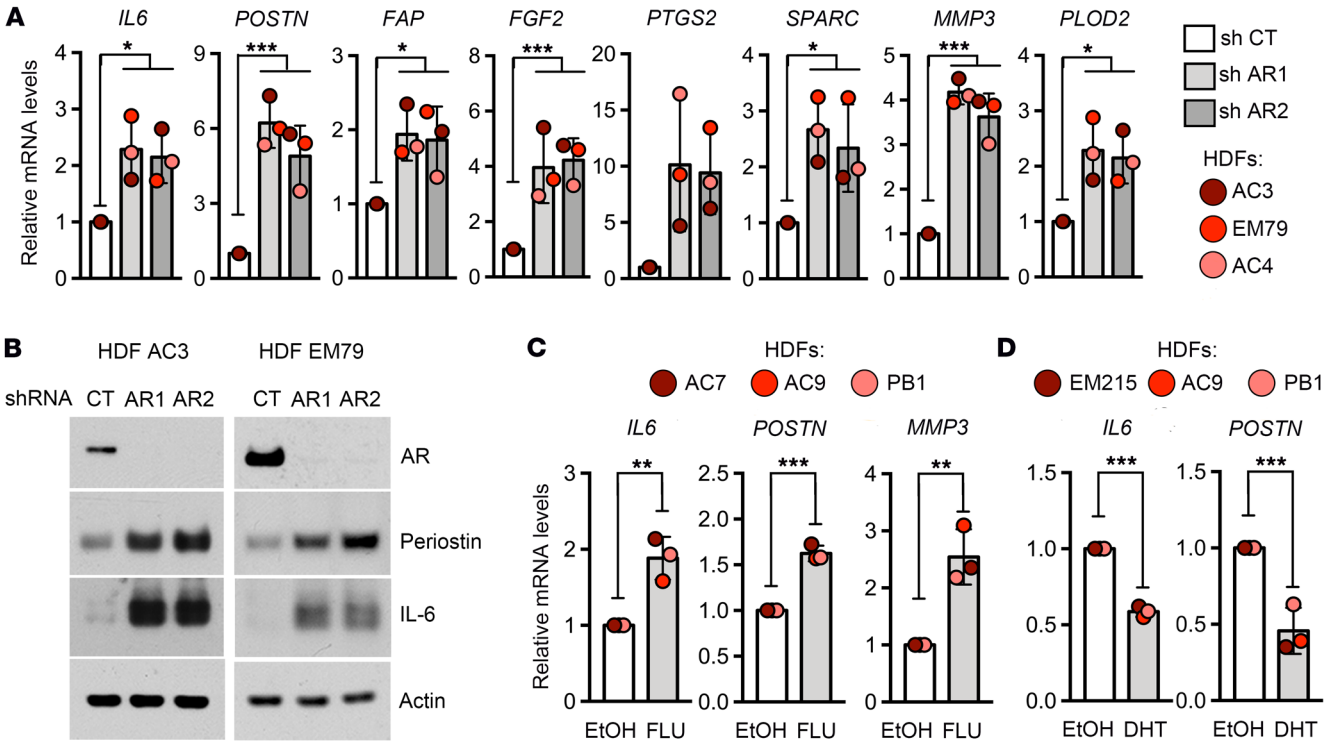

Figure 4. AR is a negative regulator of CAF effector genes. (**A**) RT-qPCR analysis of the indicated CAF effector genes in 3 HDF strains stably infected with 2 different *AR*-silencing lentiviruses (sh AR1, AR2) versus control vector (sh CT). Values for each strain are indicated as dots with mean ± SD. *n*(HDF strains) = 3; $^{*}P < 0.05$, $^{***}P < 0.005$, 1-way ANOVA with Dunnett's test. (**B**) Immunoblot analysis of periostin and IL-6 levels in 2 HDF strains with *AR*-silencing lentiviruses (sh AR1, AR2) versus control vector (sh CT). Blots were sequentially probed for AR, periostin, IL-6, and β-actin. (**C** and **D**) RT-qPCR analysis of *IL6*, *POSTN* (**C** and **D**), and *MMP3* (**C**) mRNA levels in 3 HDF strains treated with the AR antagonist flutamide (FLU; 1 μM, for 48 hours) (**C**) or with the AR agonist dihydrotestosterone (DHT; 20 nM, 24 hours) (**D**) in parallel with ethanol (EtOH) vehicle alone. Values for each patient are indicated as dots with mean ± SD. Treatment with AR agonist MK-2866 in HDFs and DHT in CAFs is shown in Supplemental Figure 3, C–E. Flutamide treatment, *n*(HDF strains) = 3; DHT treatment, *n*(HDF strains) = 3; $^{**}P < 0.01$, $^{***}P < 0.005$, 2-tailed unpaired *t* test.

HDFs with reduced AR expression promote SCC and melanoma formation. An important question was whether loss of AR expression, as observed in CAFs from skin SCCs and melanomas, is of functional significance in vivo. We addressed this question using an orthotopic model of skin cancer formation (5), based on mouse ear injections of cancer cells in combination with HDFs with or without *AR* gene silencing. HDFs with silenced *AR* significantly enhanced tumor formation of skin-derived SCC cells (SCC13) relative to control HDFs (Figure 7A). The Ki67 proliferative index of cancer cells was increased by HDFs with silenced *AR* (Figure 7B), while squamous differentiation markers (K10 and filaggrin) were reduced (Figure 7, C and D). Consistent with the in vitro results, in vivo HDFs with silenced *AR* also showed enhanced αSMA positivity and periostin production (Figure 7, E and F) and p53 upregulation (Supplemental Figure 4A). Lesions formed in the presence of *AR*-silenced fibroblasts were also characterized by increased macrophage infiltration as well as angiogenesis, as assessed by immunofluorescence with the CD68 and CD31 markers, respectively (Supplemental Figure 4, B and C).

Similar in vivo ear injection assays were repeated with another SCC cell line (CAL27) admixed with HDFs with or without *AR* knockdown. Lesions formed in the presence of fibroblasts with silenced *AR* were characterized by a higher cancer cell proliferative index and enhanced periostin deposition, macrophage infiltration, and angiogenesis (Supplemental Figure 5, A and D).

The strong downmodulation of AR in melanoma-derived CAFs suggested that it could be of functional significance also for this tumor type. To test this possibility, HDFs with or without *AR* silencing were admixed with SK-MEL-23 melanoma cells concomitantly expressing 2 fluorescent protein indicators of different phases of the cell cycle (Figure 8A and Supplemental Figure 6C; ref. 28). Monitoring of the fluorescent signals every 3 days for 4 weeks showed much greater expansion of melanoma cells in the presence of HDFs with AR silencing versus control (Figure 8A). Enhancement of tumor formation by HDFs with silenced *AR* was also observed in similar experiments with a second melanoma cell line, SK-MEL-28 (Figure 8B). Combined immunofluorescence and histochemical analysis of the lesions showed a parallel increase of melanoma cell density and proliferative index, as assessed by the MITF and Ki67 markers, respectively, as well as the lentivirally transduced GFP indicator of the S/G_2 phases of the cell cycle (ref. 28; Figure 8, C and D; and Supplemental Figure 6, A–C). These were associated with increased macrophage recruitment and vascularization, as assessed by immunofluorescence for the CD68 and CD31 markers, respectively (Supplemental Figure 6, D and E).

Thus, in an orthotopic model of skin cancer, AR loss in dermal fibroblasts significantly promotes growth of SCC and melanoma cells, enhancing at the same time angiogenesis and inflammation.

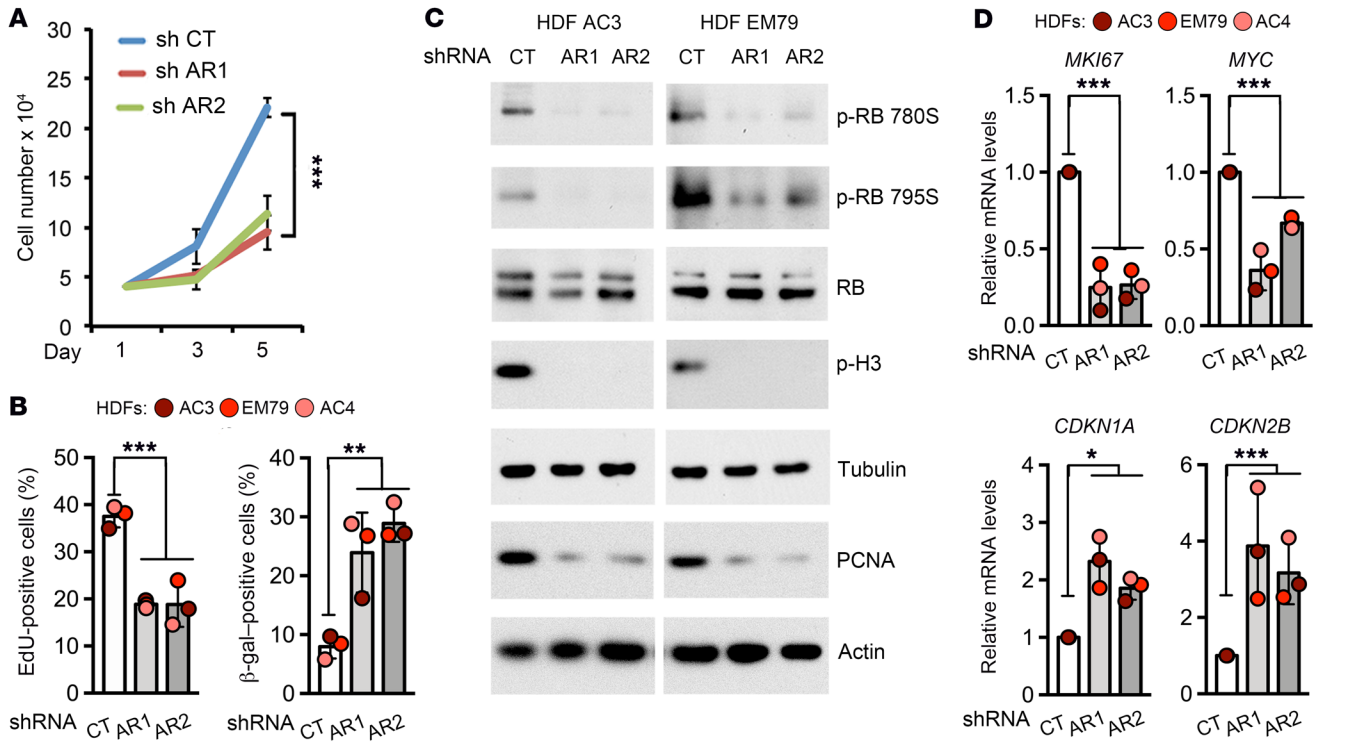

Figure 5. *AR* gene silencing in HDFs reduces proliferation and induces senescence. (**A**) Growth curve of 3 HDF strains with *AR*-silencing lentiviruses (sh AR1, AR2) versus control vector (sh CT). An equal number of cells were plated onto dishes 9 days after lentiviral infection and antibiotic resistance selection, followed by cell number determination at the indicated times (days) after plating. Data are expressed as mean values of the 3 strains ± SD. *n*(HDF strains) = 3; ***$P < 0.005$, 1-way ANOVA with Dunnett's test. (**B**) Left: EdU labeling assays of 3 HDF strains 10 days after infection with *AR*-silencing lentiviruses (sh AR1, AR2) versus control vector (sh CT). Right: Senescence-associated β-galactosidase staining of 3 HDF strains with *AR*-silencing lentiviruses (sh AR1, AR2) versus control vector (sh CT) 10 days after lentiviral vector infection. At least 200 cells per condition were scored. Values for each strain are indicated with mean ± SD. *n*(HDF strains) = 3; **$P < 0.01$,***$P < 0.005$, 1-way ANOVA with Dunnett's test. (**C**) Immunoblot analysis of 2 HDF strains infected with *AR*-silencing lentiviruses (sh AR1, AR2) versus control vector (sh CT), with antibodies against the indicated proteins. Blots were sequentially probed with antibodies against phospho-Ser795 RB, phospho–Ser780 RB, phospho-H3, RB, and γ-tubulin. A separate membrane was probed with antibodies against PCNA and β-actin. (**D**) RT-qPCR analysis of the indicated genes in 3 HDF strains infected with *AR*-silencing lentiviruses (sh AR1, AR2) versus control vector (sh CT). Values for each strain are indicated with mean ± SD. *n*(HDF strains) = 3; *$P < 0.05$, **$P < 0.01$, ***$P < 0.005$, 1-way ANOVA with Dunnett's test.

AR and CSL converge on negative control of CAF activation. AR controls transcription in both a positive and a negative manner (15). By RNA-Seq analysis, we found a consistent up- and downregulation of several hundred genes in 2 different HDF strains with *AR* silencing versus controls (Supplemental Table 1). Gene ontology analysis showed that upregulated genes were significantly enriched for functions related to extracellular matrix, wounding, and immune and inflammatory responses, while downregulated genes were enriched for nuclear functions related to nucleosome organization, transcription, and other nuclear and RNA biosynthetic processes (Supplemental Figure 7A and Supplemental Table 1).

Gene set enrichment analysis (GSEA) allows an unbiased comparison of gene expression profiles with previously established gene signatures (29). Using this approach, we found a significant association between the profile of upregulated genes in HDFs with *AR* knockdown and a signature of CAF effector genes as well as a more extended signature of *CSL* gene silencing, a critical repressor of CAF activation (refs. 5, 6 and Supplemental Figure 7B). In keeping with this finding, the profile of upregulated genes in HDFs with *AR* knockdown was also significantly associated with other signatures of relevance to CAF activation under CSL control in HDFs (ref. 5 and Supplemental Table 2).

TGF-β signaling is a key pathway leading to CAF activation in multiple organs/compartments (2). Besides CAF effectors, direct comparison of RNA-Seq profiles of HDFs with AR versus CSL silencing pointed to the *TGFBR1* gene as a common AR and CSL target. RT-qPCR and immunoblot analysis confirmed that TGFBR1 expression is induced in HDFs upon AR and CSL silencing and showed that it is also upregulated in CAFs (Supplemental Figure 8, A–D). TGFBR1 levels were also increased in dermal fibroblasts underlying SCC and AK lesions, by LCM/RT-qPCR analysis and immunofluorescence, respectively (Supplemental Figure 8, E and F).

The above results raised the possibility that AR and CSL converge on transcriptional control of CAF activation. We found that the promoter and upstream regulatory regions of various CAF effector genes such as *IL6*, *POSTN*, *PLOD2*, *FAP*, and *TGFBR1* harbor a clustering of predicted AR and CSL binding sequences (Figure 9, A and B; Supplemental Figure 8G; and Supplemental Figure 9A). ChIP assays of multiple HDF strains cultured in charcoal-stripped medium (to remove serum-bound testosterone) with or without DHT treatment showed ligand-dependent binding of AR to the predicted sites (Figure 9, A and B; Supplemental Figure 8G; and Supplemental Figure 9A). In parallel, we found increased activated histone marks at these sites in HDFs with AR silencing

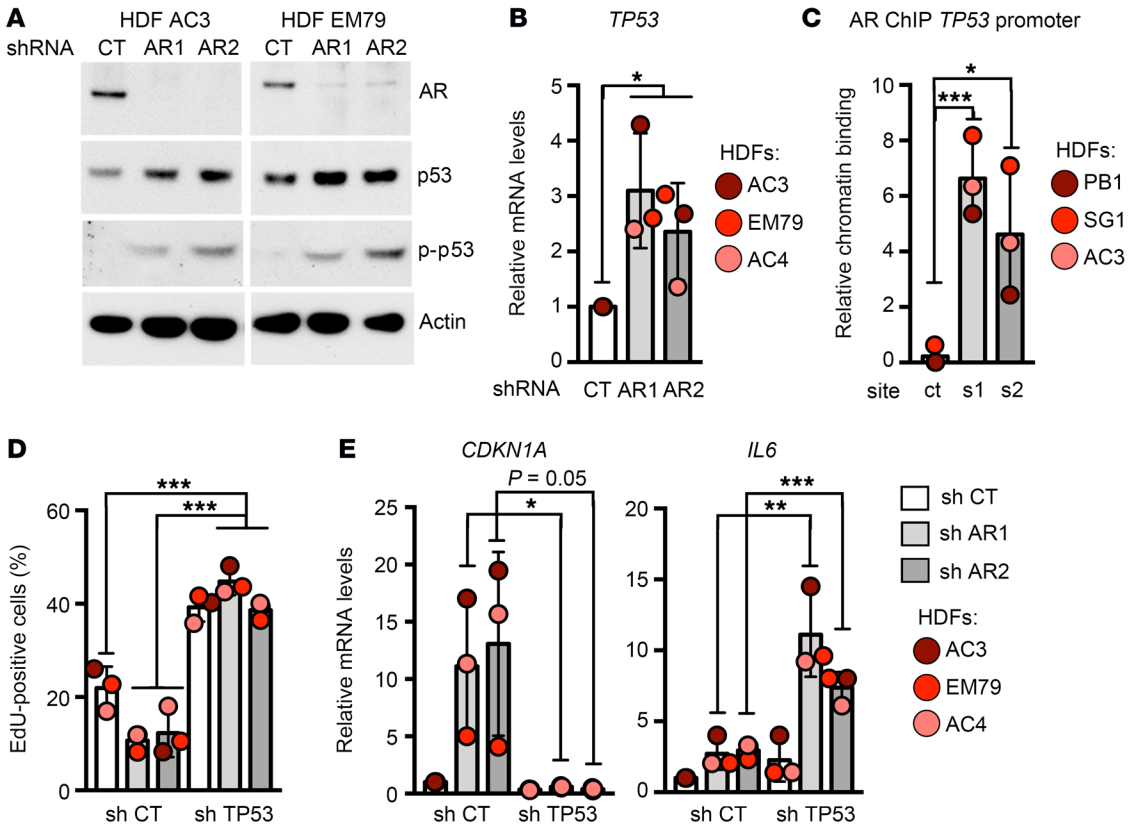

Figure 6. AR represses *TP53* gene activation. (**A**) Immunoblot analysis of p53 expression in 2 HDF strains infected with *AR*-silencing lentiviruses versus control vector. Blots were sequentially probed with antibodies against phospho–Ser15 p53, AR, p53, and β-actin. (**B**) RT-qPCR analysis of *TP53* expression in 3 HDF strains infected with *AR*-silencing lentiviruses versus control vector. Values for each strain are indicated as dots with mean ± SD. *n*(HDF strains) = 3; $^{*}P < 0.05$, 1-way ANOVA with Dunnett's test. (**C**) ChIP at *TP53* promoter, using anti-AR antibodies in parallel with nonimmune IgGs. Data are expressed as relative fold enrichment over IgGs, and values for each strain are indicated as dots with mean ± SD. Statistical significance was calculated between AR enrichment at the indicated sites relative to the flanking control region. *n*(HDF strains) = 3; $^{*}P < 0.05$, $^{***}P < 0.005$, 1-way ANOVA with Dunnett's test. (**D**) EdU labeling assays of 3 HDF strains stably infected with a *TP53*-silencing retrovirus (sh TP53) versus control vector (sh CT), with or without subsequent *AR* gene silencing for 10 days, scoring at least 200 cells per condition. Values for each strain are indicated as dots with mean ± SD. Statistical significance was calculated on differences in changes caused by *AR* silencing in cells with versus without *TP53* silencing or in cells with versus without concomitant *AR* and *TP53* silencing. *n*(HDF strains) = 3; $^{***}P < 0.005$, 1-way ANOVA with Dunnett's test. (**E**) RT-qPCR analysis of the indicated genes in 3 HDF strains infected as in **D** with a *TP53*-silencing retrovirus (sh TP53) versus control vector (sh CT), with or without subsequent *AR* gene silencing. Values for each strain are indicated as dots with mean ± SD. *n*(HDF strains) = 3; $^{*}P < 0.05$, $^{**}P < 0.01$, $^{***}P < 0.005$, 2-tailed unpaired *t* test.

(Supplemental Figure 9B) and in CAFs compared with matched HDFs (Supplemental Figure 9C). Further ChIP and re-ChIP assays, based on sequential immunoprecipitation with antibodies against CSL and AR, showed parallel binding of the AR and CSL proteins to many of these sites with concomitant binding to some of them (Figure 9C and Supplemental Figure 8H).

Such close and concomitant binding of AR and CSL to common sites suggested that the 2 proteins can be part of the same complex. In fact, an AR-CSL association could be easily visualized by proximity ligation assays (PLAs), using HDFs with silenced CSL as specificity control (Figure 10A). Similar assays were repeated with HDFs cultured in medium with charcoal-treated serum, and with or without DHT treatment, showing that AR-CSL association is ligand dependent (Figure 10B). Consistent with their decreased AR and CSL levels, the number of PLA-positive puncta was markedly reduced in a set of CAFs when compared with matched normal skin HDFs derived from the same patients (Supplemental Figure 10A).

Coimmunoprecipitation experiments with antibodies against either AR or CSL followed by reciprocal immunoblotting confirmed association of the 2 endogenous proteins in HDFs (Figure 10C). In addition, 2 long noncoding RNAs (lncRNAs) involved in control of chromatin organization that directly interact with AR, *HOTAIR* and *SRA* (steroid receptor RNA activator) (30, 31), were also found to associate with CSL, while no association was found with an unrelated lncRNA, *H19*, or *GAPDH* mRNA control (Figure 10D).

Thus, AR converges with CSL in negative control of CAF effector genes as part of the same complex.

Concordant downmodulation of AR and CSL in CAFs and counteracting impact of BET inhibitors and AR overexpression. Robust biological systems depend on coordinated control of key network elements. Parallel downmodulation of AR and CSL in dermal fibroblasts underlying premalignant and malignant skin cancer lesions and various CAFs raised the possibility of a reciprocal cross-regulation. Immunoblot and RT-qPCR analysis showed consistent suppression of AR expression, at both mRNA and pro-

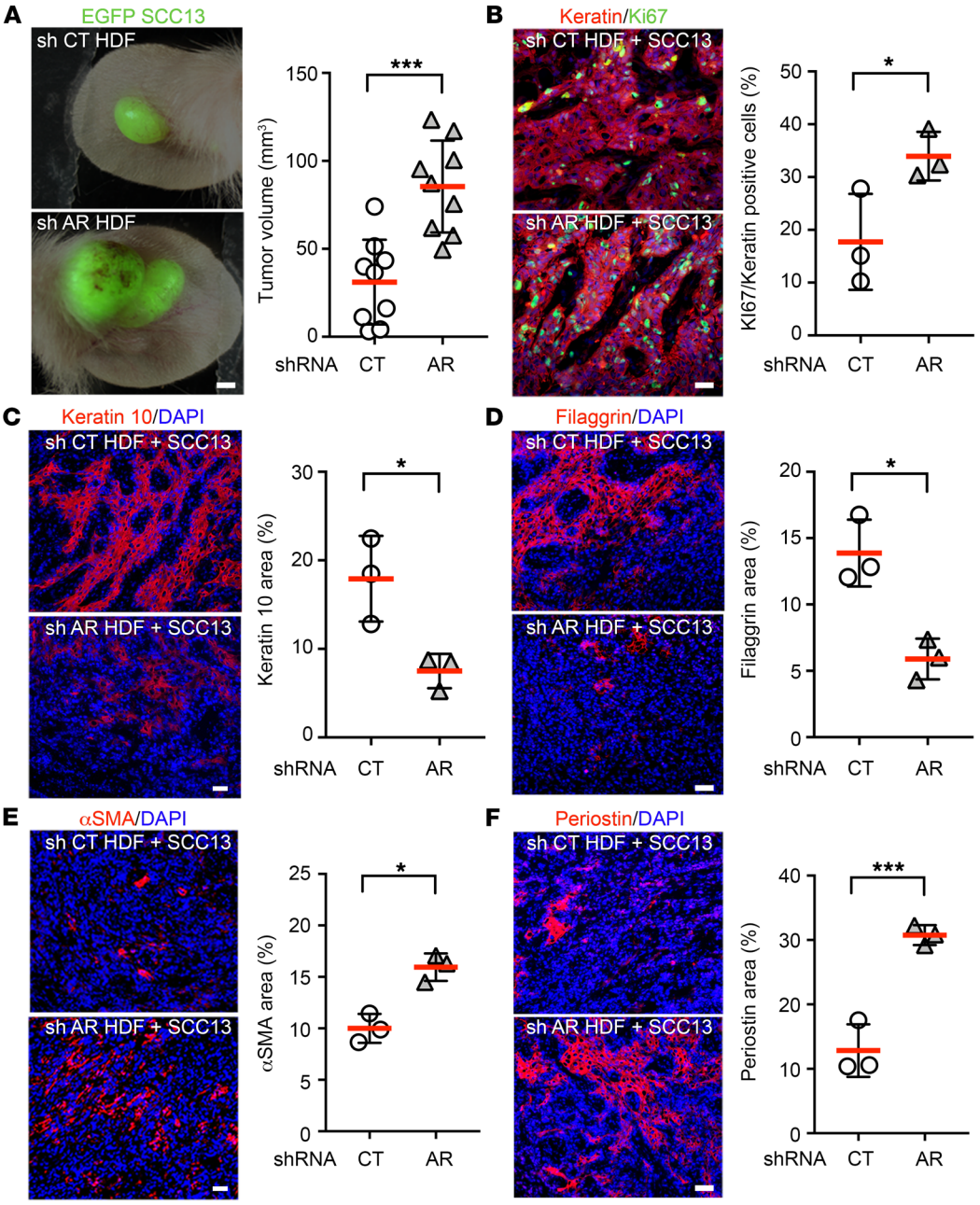

Figure 7. HDFs with reduced AR expression favor SCC cell growth in vivo. (**A**) EGFP-expressing SCC13 cells were admixed with 2 different HDF strains with silenced *AR* versus control, followed by parallel injections into contralateral ears of NOD/SCID/IL2rg$^{-/-}$ mice (8–10 weeks old, females). Left: Representative images of combined bright-field and fluorescence microscopy of 1 pair of mouse ear lesions, at 21 days after injection. Scale bar: 1 mm. Right: Quantification of tumor volumes (V = length × width × 0.5) formed in the presence of HDFs with silenced *AR* versus control. Data are represented as mean ± SD. n(tumor pairs) = 9; ***$P < 0.005$, 2-tailed paired t test. (**B**) Immunofluorescence analysis and quantification of Ki67- and keratin-positive cells in lesions formed by SCC13 cells admixed with HDFs with or without *AR* silencing. Shown are representative images and quantification for 3 ear pairs, examining at least 4 independent fields per lesion, using ImageJ software for determination of Ki67/keratin–double-positive cells. Scale bar: 30 μm. Data are represented as mean ± SD. n(tumor pairs) = 3; *$P < 0.05$, 2-tailed paired t test. (**C**–**F**) Immunofluorescence analysis and quantification of the indicated markers in lesions formed by SCC13 cells admixed with HDFs with or without *AR* silencing. Shown are representative images and quantification for 3 ear pairs, examining at least 4 independent fields per lesion, using ImageJ software. Scale bars: 60 μm. Values are expressed as percentage of surface area positive for the indicated markers. Data are represented as mean ± SD. n(tumor pairs) = 3; *$P < 0.05$, ***$P < 0.005$, 2-tailed unpaired t test. Additional data for p53, macrophage, and angiogenesis markers and further in vivo experiment with CAL27 SCC cells are shown in Supplemental Figures 4 and 5.

tein levels, in multiple HDF strains with *CSL* knockdown (Figure 11, A and B). As CSL functions as a repressor of transcription, the concomitant downmodulation of AR expression is likely to occur through an indirect mechanism and epigenetic changes like those we previously reported in HDF with decreased CSL levels (6). In fact, ChIP analysis of HDFs with *CSL* gene silencing versus controls showed an increase of the repressive histone mark H3K9Me3 and a decrease of the active histone mark H3K27Ac at the *AR* pro-

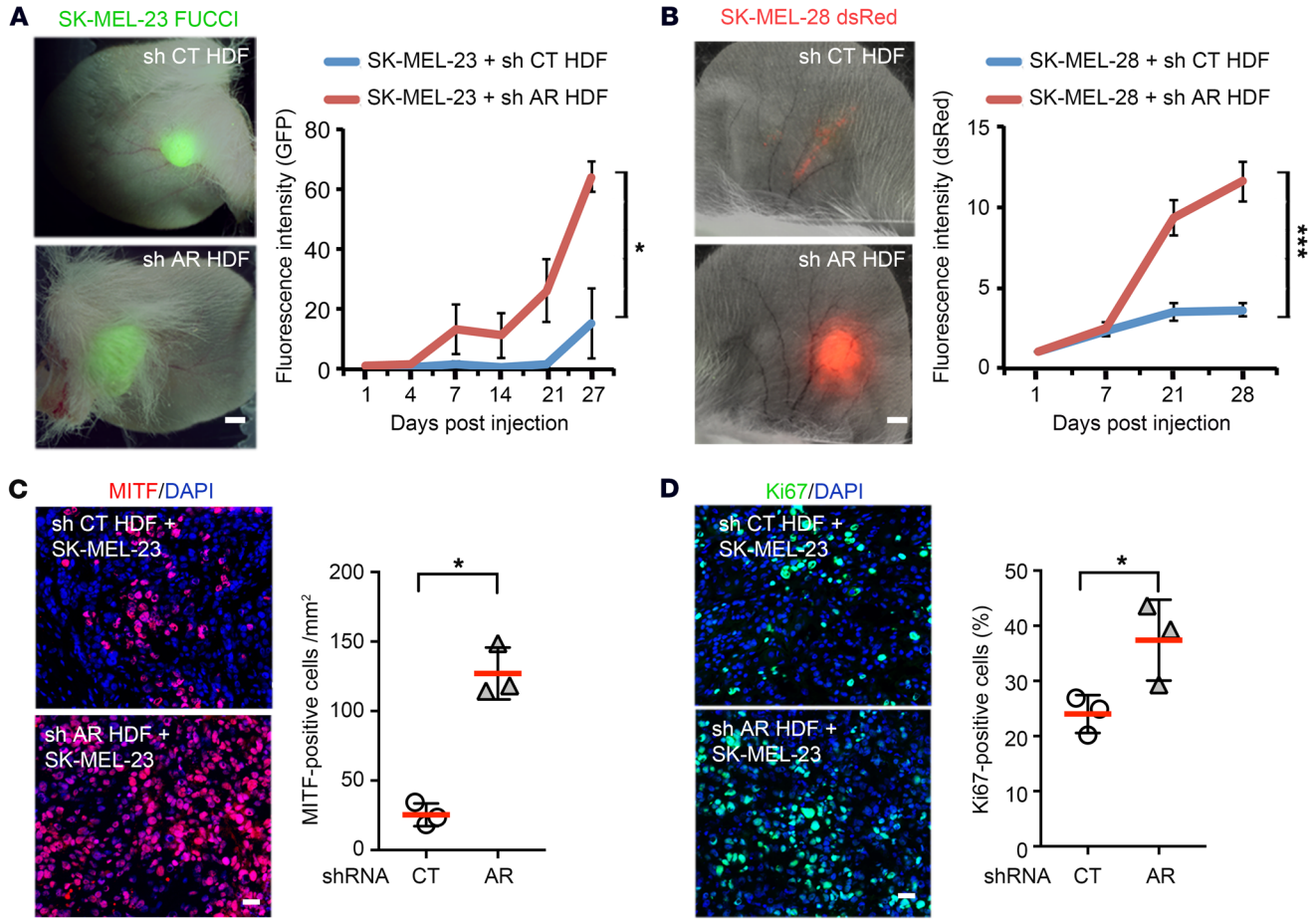

Figure 8. HDFs with reduced AR expression sustain melanoma cell growth in vivo. (**A**) SK-MEL-23 melanoma cells expressing a fluorescent indicator of cell cycle (GFP-FUCCI protein for S/G_2 phases of the cell cycle) were admixed with HDFs with silenced *AR* versus control, followed by parallel injections into contralateral ears of NOD/SCID/IL2rg$^{-/-}$ mice (8–10 weeks old, females). Shown are representative images of combined bright-field and fluorescence microscopy of a pair of mouse ears, at 27 days after injection, with quantification of the green fluorescence intensity signal (intensity × surface area) at the indicated time points after signal normalization on day 1. Scale bar: 1 mm. Data are represented as mean ± SEM. *n*(tumor pairs) = 3; **P* < 0.05, 2-tailed paired *t* test. (**B**) SK-MEL-28 melanoma cells expressing dsRed were admixed with HDFs with silenced *AR* versus control, followed by parallel injections into contralateral ears of NOD/SCID/IL2rg$^{-/-}$ mice (8–10 weeks old, male). Shown are representative images of combined bright-field and fluorescence microscopy of a pair of mouse ears, at 28 days after injection, with quantification of the red fluorescence intensity signal (intensity × surface area) at the indicated time points after injection after signal normalization on day 1. Scale bar: 1 mm. Data are represented as mean ± SEM. *n*(tumor pairs) = 5; ****P* < 0.005, 2-tailed paired *t* test. (**C** and **D**) Immunofluorescence analysis for the MITF and Ki67 markers in lesions formed by SK-MEL-23 cells admixed with HDFs with or without *AR* silencing. Shown are representative images and quantification for 3 tumor pairs, examining at least 4 independent fields per lesion, using ImageJ software. Values are expressed as number of MITF-positive melanoma cells per square millimeter (**C**) and percentage of Ki67-positive cells (**D**). Data are represented as mean ± SD. *n*(tumor pairs) = 3; **P* < 0.05, 2-tailed paired *t* test. Scale bars: 30 μm. Representative H&E staining and additional macrophage and angiogenesis markers are show in Supplemental Figure 6.

moter region, with reduced POLII recruitment and a decrease of the elongation histone mark H3K36Me in the transcribed gene body region (Figure 11C).

An attractive possibility was also that AR expression in turn controls CSL expression. In fact, combined immunoblot and RT-qPCR analysis showed that in multiple HDF strains *AR* gene silencing caused a consistent downmodulation of CSL expression only at the protein level, without any effects on the mRNA (Figure 11, D and E).

Further studies on joint control of AR and CSL expression will have to be separately pursued. Here we focused on the possible translational implications of the findings for reversion of the CAF phenotype. The global effects of CSL loss on CAF activation are counteracted by treatment with BET protein inhibitors that interfere with the impact of chromatin modifications on the basal transcription complex (6). GSEA analysis of the gene expression profiles of several CAF strains treated with JQ1 showed a suppression of the *AR* gene silencing signature (Supplemental Figure 11A). Underlying these changes, we found that treatment of CAF as well as HDF strains with JQ1 and 2 other BET inhibitors (iBET-762 and OTX-015) under clinical trials (32) induced AR expression at both the mRNA and protein levels (Figure 12, A–C, and Supplemental Figure 11, B–D).

We previously reported that topical treatment with JQ1 in the mouse ear orthotopic model suppresses CAF activation and SCC cell expansion (6). Similar assays with SK-MEL-23 melanoma cells admixed with CAFs showed even more pronounced effects of JQ1 treatment, with strong suppression of tumor growth that made

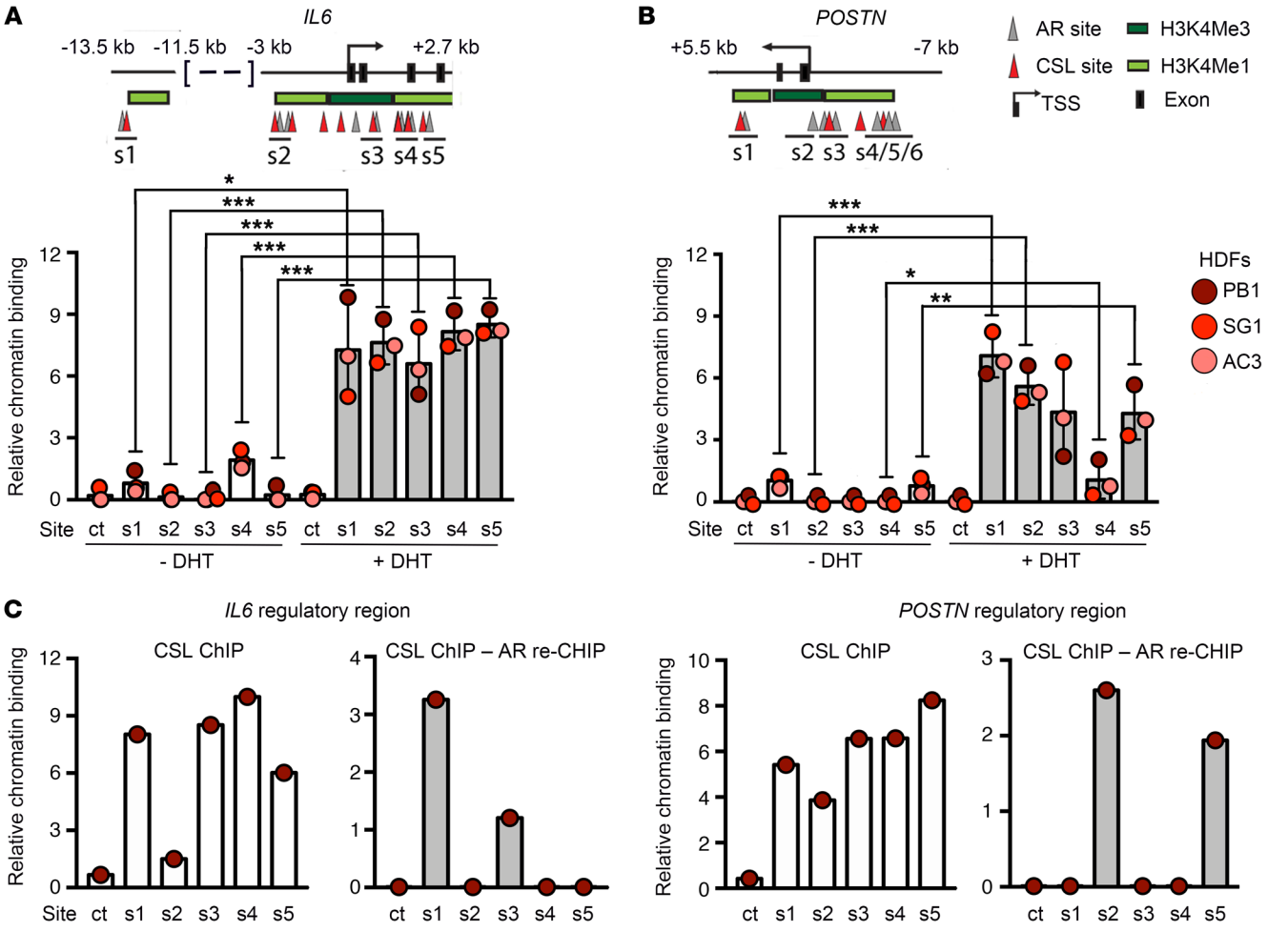

Figure 9. AR and CSL converge on negative control of CAF effector genes. (**A**) Top: Map of predicted AR and CSL binding sites (gray and red arrowheads, respectively) on the selected regions of the *IL6* gene encompassing the promoter and a distant enhancer. Areas enriched for the H3K4Me3 (dark green) and H3K4Me1 (light green) histone marks (obtained from ENCODE tracks for HDFs) are also indicated. s1–s5 indicate the sites selected for analysis. Bottom: ChIP assay at the indicated sites of the *IL6* gene, as shown in the previous panel, together with a region 11 kb upstream from the transcription start site devoid of AR recognition sequence as negative control (ct), using 3 different HDF strains cultured in charcoal-stripped medium (to remove serum-bound testosterone) with or without treatment with DHT (10 nM, 24 hours). Data are expressed as relative fold enrichment over IgGs, and values for each strain are indicated as dots with mean ± SD. Statistical significance of differences in AR enrichment with versus without DHT treatment at the indicated sites was calculated. *n*(HDF strains) = 3; $^{*}P < 0.05$, $^{***}P < 0.005$, 2-tailed unpaired *t* test. (**B**) Map of predicted AR and CSL binding sites on the *POSTN* promoter regulatory region and determination of AR binding by ChIP in the absence or presence of the AR agonist DHT (10 nM, 24 hours) as in **A**. *n*(HDF strains) = 3; $^{*}P < 0.05$, $^{**}P < 0.01$, $^{***}P < 0.005$, 2-tailed unpaired *t* test. (**C**) Determination of CSL and CSL-AR binding on the indicated sites of the *IL6* and *POSTN* genes, by ChIP and re-ChIP assays based on immunoprecipitation with anti-CSL antibodies alone or sequentially with anti-AR antibodies (white and gray bars, respectively). Data are expressed as relative fold enrichment over IgGs. Additional ChIP data are available in Supplemental Figures 7–9.

it difficult to obtain tissue sections of the JQ1-treated lesions for analysis (Figure 12D). Importantly, JQ1 treatment of SK-MEL-23 cells in vitro did not significantly affect their growth (Supplemental Figure 11, E and F), pointing to the importance of the impact of this compound on tumor–stromal cell interaction.

To assess whether increased AR expression is by itself sufficient to reproduce the BET inhibitor impact on CAFs, we infected these cells with an AR-overexpressing lentivirus. Increased AR expression resulted in the consistent suppression of multiple CAF effector genes that are induced by AR and CSL loss (Figure 13, A and B, and Supplemental Figure 12A). Importantly, downmodulation of these genes by increased AR levels occurred in the absence of *CSL* upregulation, which was rather suppressed. Concomitantly, expression of the *HES1* gene, a negative CSL target in fibroblasts and CAFs (5), was also unaffected or even induced by AR overexpression (Figure 13, A and B), indicating that increased AR levels can suppress CAF effector genes, short-circuiting the consequences of CSL loss.

In parallel with the above results, AR overexpression suppressed the ability of CAFs to enhance proliferation and stem cell potential of neighboring SCC13 cancer cells, as assessed by conventional cocultures and 3D sphere-forming assays, respectively (Figure 13, C and D). Even in vivo, tumorigenic expansion of SCC13 cells was significantly decreased when they were admixed with AR-overexpressing CAFs in comparison with controls (Figure 14A). This was accompanied by a lower proliferative index of cancer cells and enhanced squamous differentiation with reduced CAF marker expression, angiogenesis, and macrophage infiltration (Figure 14, B–F, and Supplemental Figure 12, B and C).

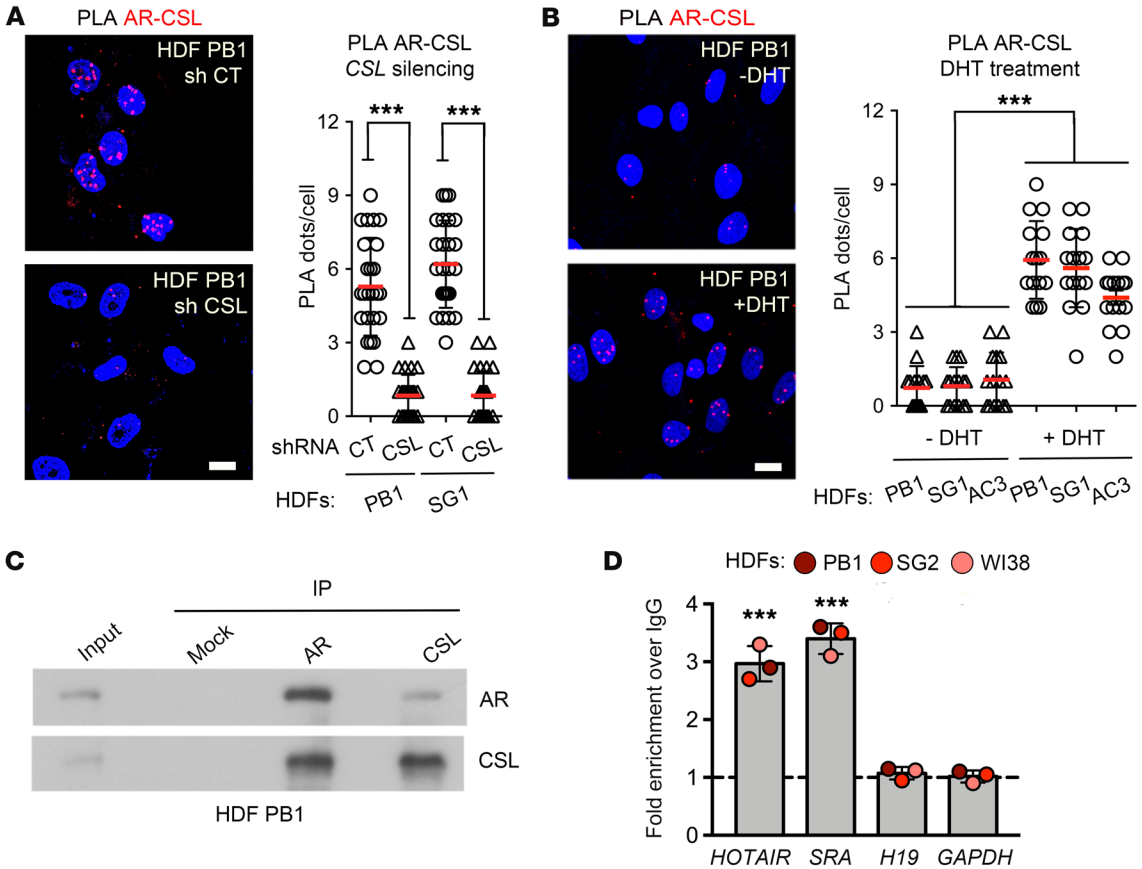

Figure 10. AR and CSL physically interact in primary HDFs. (**A**) Proximity ligation assays (PLAs) with antibodies against AR and CSL of 2 HDF strains with or without CSL gene silencing as specificity control. Red fluorescence puncta resulting from the juxtaposition of anti-AR and anti-CSL antibodies were visualized by confocal microscopy with concomitant DAPI nuclear staining. Shown are representative images and quantification of number of puncta per cell. Scale bar: 10 μm. Values of PLA puncta for each individual cell are indicated with mean ± SD. *n*(cell measurements per condition) = 35; ***$P < 0.005$, 2-tailed unpaired *t* test. (**B**) PLAs with antibodies against AR and CSL in 3 HDF strains in the absence or presence of the AR agonist DHT (10 nM, 24 hours). Scale bar: 10 μm. Values of PLA puncta for each individual cell are indicated with mean ± SD. *n*(HDF strains) = 3, *n*(CAF strains) = 3; ***$P < 0.005$, 2-tailed unpaired *t* test. Additional PLAs carried out in HDFs versus CAFs are shown in Supplemental Figure 10. (**C**) Reciprocal coimmunoprecipitation assays of CSL and AR association. HDF total cell extracts were immunoprecipitated with anti-AR or anti-CSL rabbit polyclonal antibodies or nonimmune IgG (mock). Immunoblotting was carried out with anti-AR or anti-CSL mouse monoclonal antibodies. (**D**) Total cell extracts of 2 HDF strains and WI38 lung fibroblasts were processed for RNA immunoprecipitation with anti-CSL antibodies versus nonimmune IgGs. Immunoprecipitated RNAs were analyzed by RT-qPCR with specific primers for *HOTAIR* lncRNA, *SRA* lncRNA, *H19* lncRNA, and *GAPDH* mRNA. Results are expressed as fold enrichment in immunoprecipitates with anti-CSL antibodies versus nonimmune IgG (dashed line), and values for each HDF strain are indicated as dots with mean ± SD. *n*(fibroblast strains) = 3; ***$P < 0.005$, 2-tailed unpaired *t* test.

Thus, AR is coordinately controlled with CSL, and its upregulation is of translational significance for suppression of CAF activation and stroma-focused anticancer intervention.

Discussion

Conversion of stromal fibroblasts into CAFs is likely to occur as a multistep process with concomitant deregulation of several pathways (2, 5, 6, 33). Surprisingly, the impact of hormone signaling in this context has been explored to a very limited extent (7). AR is functionally involved in various aspects of cell and tissue homeostasis in organs with both reproductive and nonreproductive functions (15). Levels of androgens decline with age (34), suggesting that decreased AR signaling contributes to various aspects of the aging process, including tissue atrophy and impaired metabolic functions (34, 35). Whether decreased AR signaling is also a determinant of cancer risk remains to be established.

We focused on skin cancer, as a benchmark of major clinical significance for cancer development. We found that AR levels are downmodulated in CAFs derived from all 3 major skin cancer types, SCC, BCC, and melanoma, and are already reduced in stromal fibroblasts underlying premalignant AK and dysplastic nevus lesions. Decreased AR expression is of functional importance as it is sufficient to trigger dermal fibroblasts to CAF activation, with consequent enhancement, in an orthotopic model of both SCC and melanoma tumor expansion.

The AR protein can act as either repressor or activator of gene transcription, depending on cell type, target genes, and proteins with which it associates (15). Loss of AR expression in multiple independent HDF strains, from both male and female donors, led to induction of key CAF effector genes, with a similar induction in fibroblasts from other body sites, indicating that AR is likely to play a general repressive function in CAF activa-

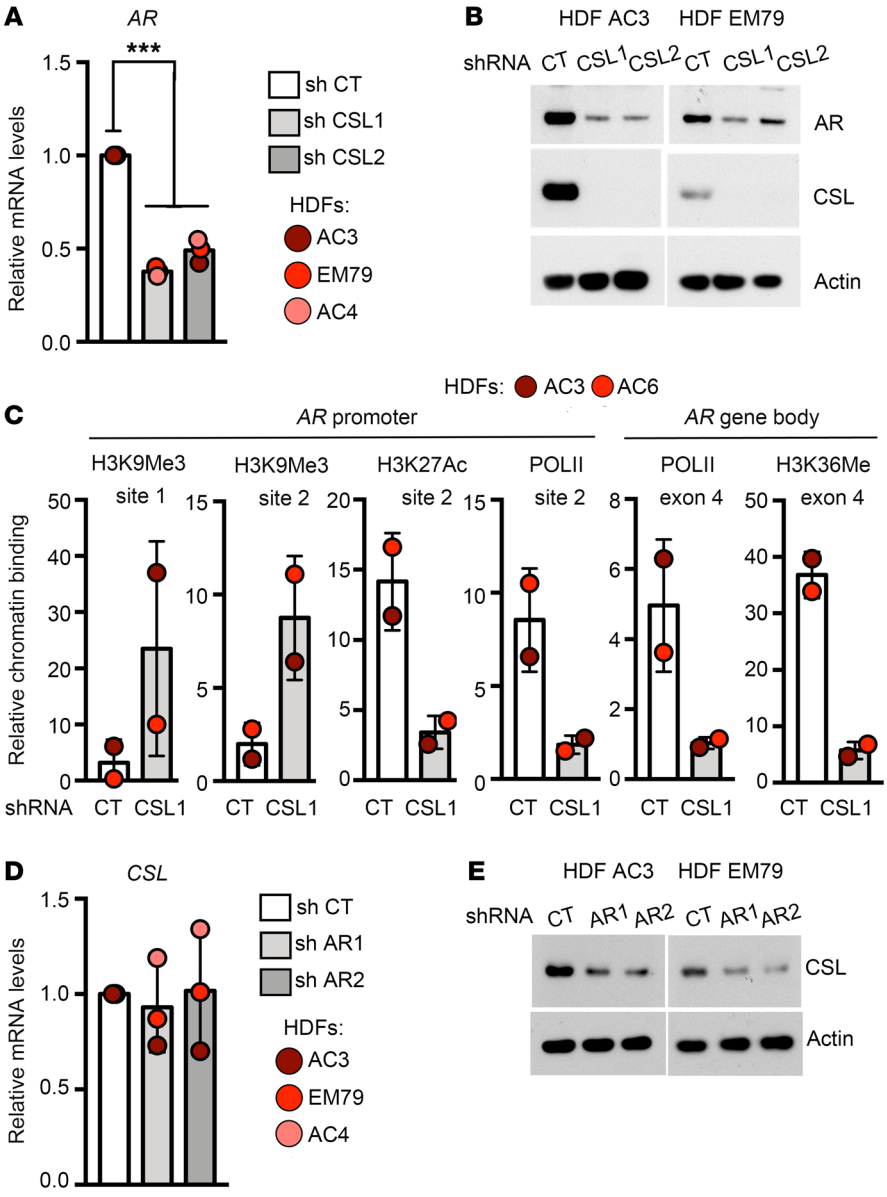

Figure 11. Reciprocal regulation of AR and CSL expression in HDFs. (**A**) RT-qPCR analysis of *AR* mRNA expression in 3 independent HDF strains stably infected with 2 different *CSL*-silencing lentiviruses (sh CSL1, CSL2) versus control vector (sh CT). Values for each strain are indicated as dots with mean ± SD. *n*(HDF strains) = 3; ***$P < 0.005$, 1-way ANOVA with Dunnett's test. (**B**) Immunoblot analysis of AR levels in 2 HDF strains stably infected with 2 different *CSL*-silencing lentiviruses (sh CSL1, CSL2) versus control vector (sh CT). Blots were sequentially probed for AR, CSL, and β-actin. (**C**) ChIP assay determination of H3K9Me3, H3K27Ac, POLII, and H3K36Me binding to the *AR* promoter and transcribed gene body regions (identified by ENCODE) in 2 HDF strains with or without *CSL* gene silencing. Data are expressed as relative fold enrichment over IgGs, and values for each strain are indicated as dots with mean ± SD. *n*(HDF strains) = 2. (**D** and **E**) Analysis of CSL expression by RT-qPCR (**D**) and immunoblotting (**E**) of multiple HDF strains stably infected with 2 *AR*-silencing lentiviruses (sh AR1, AR2) versus control vector (sh CT). For RT-qPCR analysis, values for each strain are indicated as dots with mean ± SD. *n*(HDF) = 3. Blots were sequentially probed for CSL and β-actin.

tion. Paralleling the genetic findings, treatment of normal fibroblasts with flutamide, a selective antagonist that competes with androgens for AR binding and activation (26), resulted in induction of CAF effector genes, while expression of these genes was suppressed by AR agonists.

While androgen signaling promotes differentiation in normal prostate tissue (36), androgen deprivation therapy (ADT) is the mainstay treatment of metastatic prostate cancer (26). Even in this context, however, inhibition of AR signaling has been reported to promote rather than suppress malignant progression of prostate cancer cells (37) and prostate cancer relapse through an impact on T cell activation (38), a concern that may extend to cancer stromal fibroblasts. In this context, we also note a reported association between melanoma incidence and previous history of prostate cancer, even if it was not determined whether prostate cancer patients were subjected to ADT (39, 40). In addition, a positive correlation between ADT of prostate cancer patients and subsequently increased incidence of colorectal cancer was reported (41, 42).

The functional involvement of AR loss in early steps of CAF activation is strikingly similar to that of CSL. Reduction of both AR and CSL expression leads to p53-dependent cellular senescence. Mechanistically, while CSL inhibits p53 activity through direct binding (5), AR suppresses p53 expression, with p53 as direct negative target. AR and CSL converge also on negative control of CAF effector genes, binding concomitantly to neighboring sites. Physical association of the 2 proteins, as detected by proximity ligation and coimmunoprecipitation assays, suggests that they are part of a common transcription-repressive complex, which is ligand dependent. In support of this possibility, *HOTAIR* and *SRA*, 2 regulatory lncRNAs that interact with AR (30, 31), were found to associate also with CSL.

AR and CSL are concomitantly reduced at early steps of CAF activation. Parallel downmodulation of the two can be reinforced by the reciprocal regulatory loop that we have uncovered, whereby silencing of one gene resulted in suppression of the other. As CSL functions as a repressor of gene transcription, concomitant downmodulation of AR must occur through an indirect mechanism

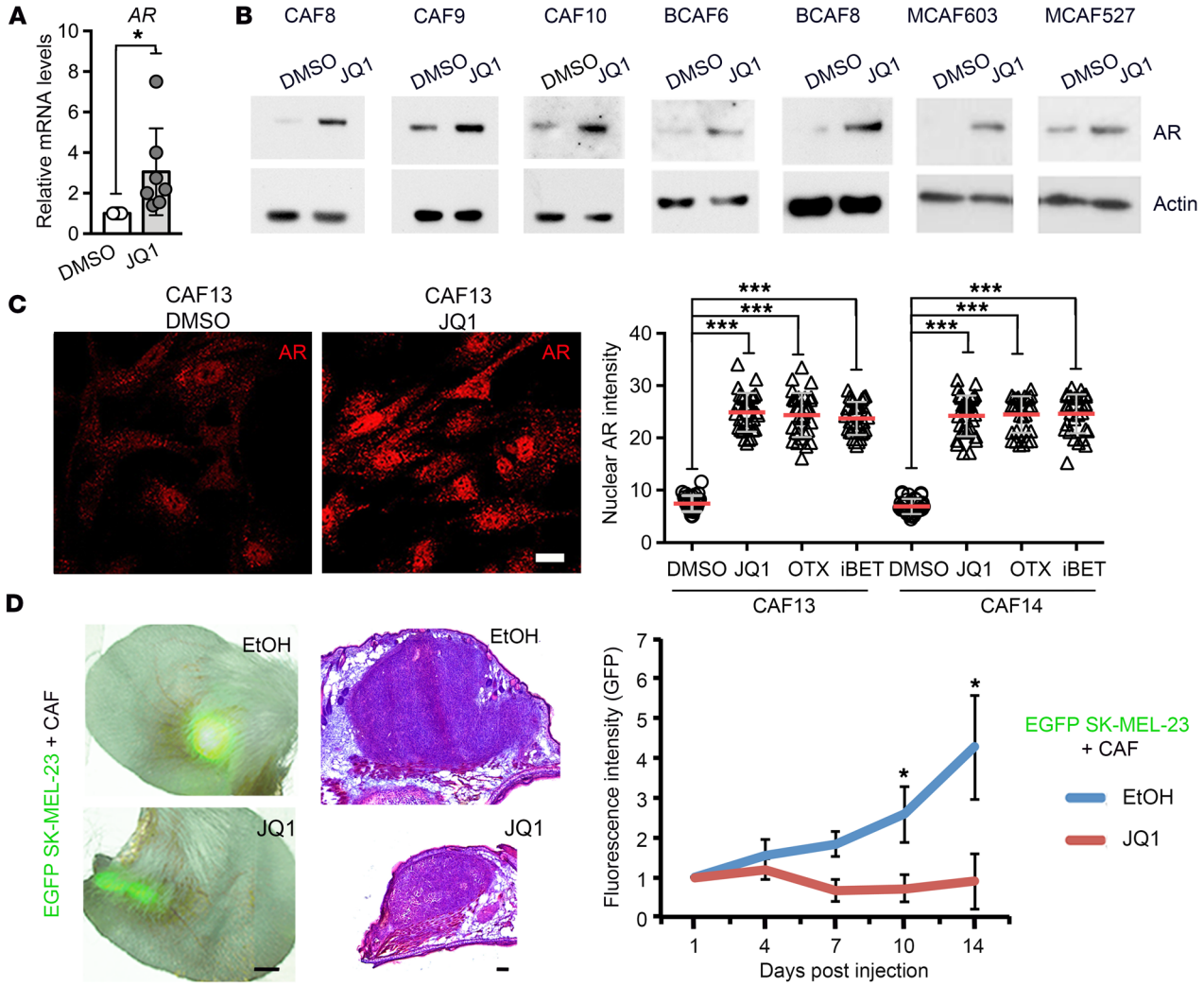

Figure 12. BET inhibitor treatment rescues AR expression in CAFs. (**A**) RT-qPCR analysis of *AR* mRNA expression in 7 SCC-derived CAF strains treated with JQ1 (100 nM) versus DMSO vehicle alone for 24 hours. Values for each strain are indicated as dots with mean ± SD. *n*(CAF strains) = 7; **P* < 0.05, 2-tailed unpaired *t* test. (**B**) Immunoblot analysis of AR expression in multiple CAF strains derived from SCC (CAF8–CAF10), BCC (BCAF6 and BCAF8), and melanoma lesions (MCAF603 and MCAF527) treated with JQ1 (100 nM) versus DMSO vehicle alone for 24 hours. (**C**) Immunofluorescence analysis of AR expression in 2 SCC-derived CAF strains treated with different BET inhibitors (JQ1, OTX, iBET; 100 nM each) versus DMSO vehicle alone for 24 hours. Representative images are shown, and AR fluorescence intensity values for each individual cell are indicated with mean ± SD. Scale bar: 10 μm. *n*(cell measurements per condition) = 35; ****P* < 0.005, 1-way ANOVA with Dunnett's test. Data on additional CAF and HDF strains are available in Supplemental Figure 11. (**D**) EGFP-expressing SK-MEL-23 melanoma cells were admixed with CAFs followed by parallel injections into contralateral ears of NOD/SCID/IL2rg$^{-/-}$ mice (8–10 weeks old, females). After 4 days, mice were treated topically biweekly with 20 μl of JQ1 as in ref. 6 or ethanol (EtOH) alone. Left panel: Representative images of combined bright-field and fluorescence microscopy of 2 mouse ear pairs at 15 days after injection. Scale bar: 1 mm. Middle panel: Representative images of H&E staining of parallel ear lesions treated with EtOH or JQ1 at the end of the experiment. Scale bar: 200 μm. Right panel: Quantification of green fluorescence intensity signal (intensity × surface area) of injected mouse ear pairs at the indicated time points after signal normalization on day 1. Data are represented as mean ± SEM. *n*(ear pairs) = 4; **P* < 0.05, 2-tailed paired *t* test.

including reported changes in other transcription factors and/or chromatin configuration (6). AR silencing resulted in decreased CSL expression only at the protein level, pointing to an impact on post-transcriptional control of this protein, through scarcely understood mechanisms that need to be further investigated.

Emerging evidence indicates that CAF activation is the result of an epigenetic process amenable to pharmacological intervention. In this context, treatment with BET inhibitors, which counteract the global gene expression changes caused by compromised CSL function in CAFs (6), restored AR expression in these cells. The findings are of likely translational significance, as increased AR expression was sufficient to short-circuit CSL loss and suppress CAF tumor-enhancing properties. AR is a highly studied target of pharmacological intervention (43, 44), and compounds leading to its increased expression and/or activity open new possibilities for stroma-focused cancer prevention and treatment.

Methods

Cell culture, cell manipulations, and treatments. HDFs, CAFs, and SCC13, CAL27, 293T, SK-MEL-28, and SK-MEL-23 cells were maintained in DMEM (Thermo Fisher Scientific) supplemented with 10% (vol/vol) FBS (Thermo Fisher Scientific) and 1% penicillin/streptomy-

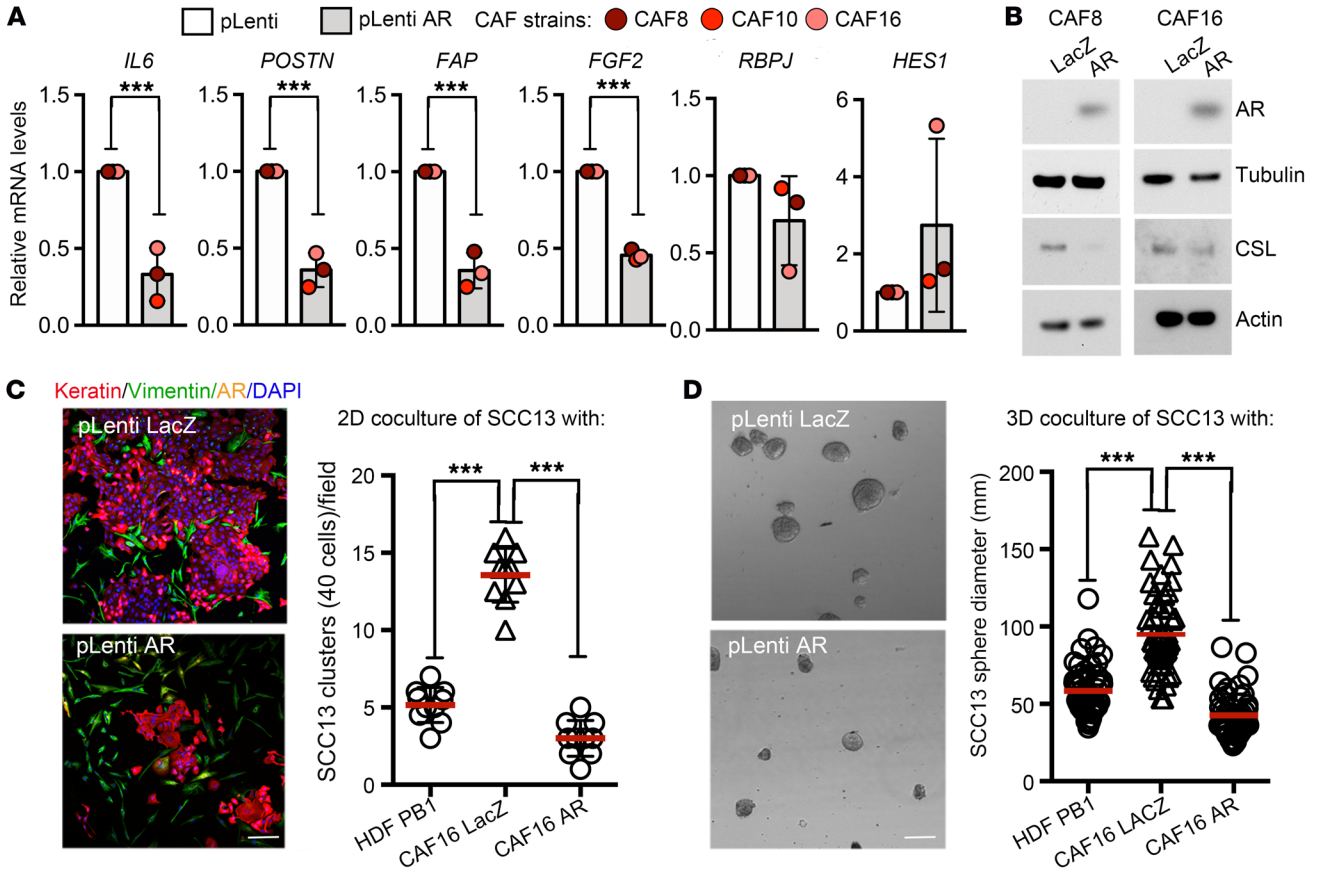

Figure 13. Reversal of CAF activation by AR overexpression. (**A**) Multiple CAF strains infected with an AR-overexpressing lentivirus (pLenti AR) versus a β-galactosidase–expressing control (pLenti LacZ) were analyzed by RT-qPCR for expression of the indicated genes. Values for each strain are indicated as dots with mean ± SD. *n*(HDF strains) = 3; ***$P < 0.005$, 2-tailed unpaired *t* test. (**B**) Immunoblot analysis of AR versus CSL protein expression in 2 CAF strains infected with an AR-overexpressing lentivirus (AR) versus control (LacZ). Blots were sequentially probed with antibodies against AR and γ-tubulin and, on a separate membrane, CSL and β-actin. αSMA regulation by AR overexpression in CAF strains is shown in Supplemental Figure 12A. (**C**) SCC13 cells were cocultured at a 1:1 ratio with HDF PB1 or CAF16 infected with β-galactosidase–expressing (pLenti LacZ) or AR-expressing (pLenti AR) lentiviruses for 3 days, followed by immunofluorescence analysis with anti-keratin (red) and anti-vimentin (green) antibodies for cell identification. Shown are representative images together with quantification of large SCC13 cell clusters (>40 cells) per examined field with mean ± SD. Scale bar: 200 μm. *n*(number of fields) = 10; ***$P < 0.005$, 1-way ANOVA with Dunnett's test. (**D**) SCC13 cells were mixed at a 1:1 ratio with HDF PB1 or β-galactosidase–expressing (pLenti LacZ) versus AR-expressing (pLenti AR) CAF16 and grown in Matrigel 3D cultures for 5 days. Shown are representative images of SCC13 spheroids together with quantification by ImageJ software of spheroid diameter with mean ± SD. Scale bar: 250 μm. *n*(number of spheroids) = 50; ***$P < 0.005$, 1-way ANOVA with Dunnett's test.

cin. Conditions of HDF and CAF isolation were previously reported (33). Human pancreatic stellate cells were maintained in stellate cell medium supplemented with 2% (vol/vol) FBS, 1% penicillin/streptomycin, and 1% stellate growth supplement (ScienCell). All cells were grown at 37°C in the humidified incubator (Thermo Fisher Scientific) with 5% CO_2. Cell lines were routinely tested to exclude mycoplasma contamination. Information regarding HDF strains and cell lines is reported in Supplemental Tables 4 and 5.

Skin SCC13 cells were originally reported in ref. 45, and CAL27 were originally provided by Genrich Tolstonog (University Hospital of Lausanne, Lausanne, Switzerland). For in vivo approaches, SCC13 and CAL27 cells were infected with an EGFP-expressing lentivirus (5), while SK-MEL-23 cells were concomitantly infected with RFP- and GFP-expressing fluorescence ubiquitination cell cycle indicator (FUCCI) viruses (28). HDF and CAF strains were stably infected with a lentiviral expression vector for constitutive expression of Myc-tagged CSL in parallel with empty vector control. CAF strains were infected with a lentiviral expression vector for constitutive expression of AR, a gift of Karl-Henning Kalland (Bergen University, Bergen, Norway), in parallel with LacZ as control. RNAi experiments were carried out using shRNA-targeting lentiviral vectors from MilliporeSigma (for *CSL*, *AR*), as previously described (5). The details of the vectors used for RNAi are given in Supplemental Table 3.

For drug treatment 24 hours after seeding, HDFs or CAFs were treated with 100 nM JQ1 (Adooq Biosciences) or DMSO as control, or 10 μM MK-2866 (Selleckchem) or EtOH as control, for 24 hours before lysis. Flutamide (1 μM) treatment (Santa Cruz Biotechnology), or EtOH as control, was carried out for 48 hours before lysis. For testosterone treatments, HDFs or CAFs were washed 4 times in PBS after seeding and left 48 hours in phenol red–free DMEM complemented with hormone-stripped FBS (Thermo Fisher Scientific) before treatment with 20 nM DHT (MilliporeSigma) for 24 hours for HDFs and for 3 or 7 days for CAFs. SK-MEL-23 melanoma cells were treated with 100 nM JQ1 (Adooq Biosciences) or DMSO for 24 hours for 5-ethynyl-2′-deoxyuridine (EdU) assay.

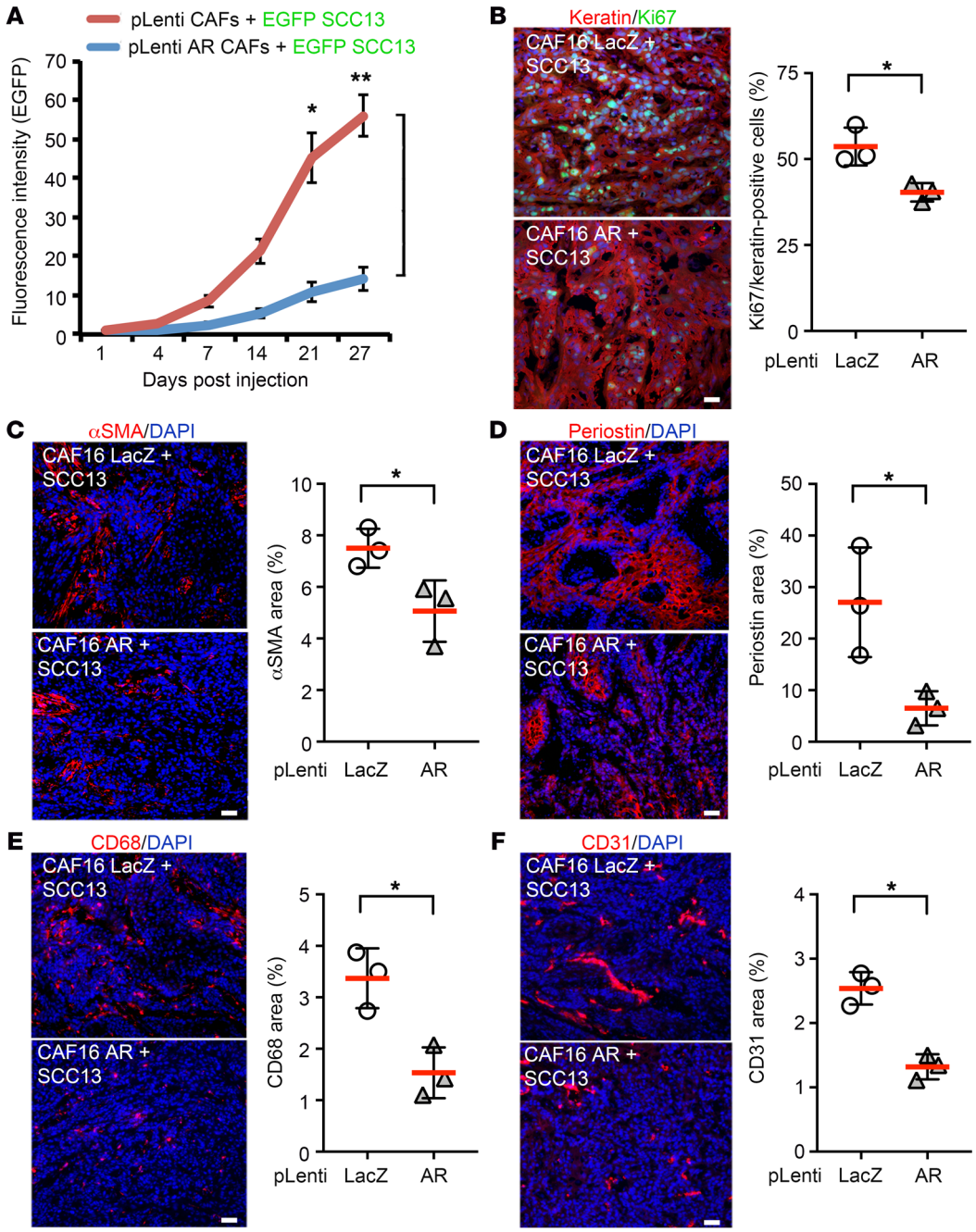

Figure 14. AR overexpression restrains in vivo CAF tumor-promoting ability. (**A**) EGFP-expressing SCC13 cells were admixed with CAFs with AR overexpression (pLenti AR) versus control (pLenti LacZ), followed by parallel ear injection into contralateral NOD/SCID/IL2rg$^{-/-}$ mice (8–10 weeks old, females). Shown is a quantification of the green fluorescence intensity signal (intensity × surface area) at the indicated time points after signal normalization on day 1. Data are represented as mean ± SEM. *n*(tumor pairs) = 7; **P* < 0.05, ***P* < 0.01, 2-tailed paired *t* test. (**B**) Immunofluorescence analysis and quantification of Ki67- and keratin-positive cells in lesions formed by SCC13 cells admixed with CAFs with or without AR overexpression. Scale bar: 30 μm. Data are represented as mean ± SD. *n*(tumor pairs) = 3; **P* < 0.05, 2-tailed paired *t* test. (**C**–**F**) Immunofluorescence analysis and quantification of the indicated markers in lesions formed by SCC13 cells admixed with CAF16 with or without AR overexpression. Shown are representative images and quantification for 3 ear pairs, examining at least 3 independent fields per lesion, using ImageJ software. Scale bars: 60 μm. Values are expressed as percentage of surface area positive for the indicated markers. Data are represented as mean ± SD. *n*(tumor pairs) = 3; **P* < 0.05, 2-tailed paired *t* test. For analysis of SCC terminal differentiation markers, see Supplemental Figure 12, B and C.

Gene expression studies, LCM, ChIP, ChIPmentation, and re-ChIP studies. Gene expression and conditions of LCM studies were carried out as previously described (5, 33).

ChIP assay for histone modification of H3K27Ac, H3K9Me3, H3K36Me, and POLII was carried out as previously described (46). ChIP tagmentation (ChIPmentation) (47) and qPCR analysis were carried out using anti-AR antibodies (Santa Cruz Biotechnology) versus nonimmune IgGs, starting from 15 × 10^6 HDFs. The immunoprecipitation of the sonicated chromatin was carried out using a previously described protocol (6). The bead-bound chromatin was tagged with

Tn5 transposase (Nextera DNA Sample Prep kit, Illumina) (47). The "tagmented" chromatin was de-cross-linked and subjected to proteinase K digestion. Equal amounts of recovered DNA (5 ng) were subjected to amplification with tag-specific primers (14 cycles). Tag-specific PCR products were diluted (1:10), and 1 μl was used as a template for qPCR to determine the enrichment of the indicated sites; the primer sequences are listed in Supplemental Table 3.

For re-ChIP assays, bead-bound chromatin samples, recovered after immunoprecipitation with either anti-CSL or nonimmune IgGs, were subjected to tagmentation and eluted in 2% SDS, 15 mM DTT in 1× TE buffer. Eluted products were diluted in immunoprecipitation buffer (Tris-HCl, pH 8.0, 1 mM EDTA, 150 mM NaCl, 0.1% Triton X-100, 1 mM PMSF, 1× protease inhibitors) and subjected to a second round of ChIP (re-ChIP) with anti-AR antibodies. After washing, the bead-bound chromatin fragments were de-cross-linked and eluted using proteinase K digestion. The eluted DNAs were amplified and subjected to ChIP-qPCR with specific primers (Supplemental Table 3) as described above. The enrichment (log_2-fold) in ChIP or re-ChIP over nonimmune IgGs is indicated as relative chromatin binding. Regulatory regions in the *IL6*, *POSTN*, *PLOD2*, *FAP*, *TGFBR1*, *TP53*, and *AR* genes were identified by loading of available track information for H3K4Me3 (for promoter) and H3K4Me1 (for enhancer elements) from data deposited in the Encyclopedia of DNA Elements at UCSC (ENCODE) for adult HDFs using the University of California, Santa Cruz (UCSC) Genome Browser (https://genome.ucsc.edu/encode/). Putative AR and CSL binding sites in the regulatory regions of the *TP53*, *IL6*, *POSTN*, *PLOD2*, *FAP*, and *TGFBR1* genes were predicted using Matinspector (Genomatix).

Cell and coculture assays, immunoblots, and immunofluorescence. Immunoblots and immunofluorescence analyses were performed as previously described (5, 33). For 2D coculture assays, SCC13 and fibroblast cells were mixed (1:1 ratio) in complete DMEM containing 10 % Matrigel (BD Biosciences) and plated onto 8-chamber glass slides (Corning). The cells were allowed to grow for 4 days in regular culture conditions. At the end of the experiment, the medium was removed from the glass slides, adherent cells were fixed with 4% paraformaldehyde and washed with PBS, and immunofluorescence staining was carried out with anti-vimentin (for fibroblasts) and anti–pan-keratin (for SCC13) antibodies. The slides were imaged using a Zeiss LSM880 confocal microscope with a ×20 objective. The images were processed in ZEN Black software, and the number of large SCC13 cell clusters (>40 cells) was counted per field manually.

For 3D coculture assays, the SCC13 and fibroblast cells were mixed and plated onto 8-well chamber slides precoated with Matrigel (BD Biosciences). In brief, 8-well chambers were coated with 100 μl Matrigel per well and incubated for 30 minutes to polymerize at 37°C. The SCC13 cells and the fibroblasts were mixed at a 1:1 ratio in complete DMEM with 1% Matrigel and overlaid on polymerized Matrigel chambers. The spheroids were allowed to grow for 6 days and analyzed using an EVOS Cell Imaging System (Thermo Fisher Scientific). The diameter of the spheroids was measured using ImageJ (NIH). See complete unedited blots for Figures 3–6, 10–13, and Supplemental Figures 3, 8, and 11 in the supplemental material.

RNA immunoprecipitation. RNA immunoprecipitation (RIP) assay was carried out as described in ref. 48 with minor modifications. Briefly, HDFs were lysed in RIP buffer (10 mM Tris-HCl, pH 7.5, 0.5% Nonidet P-40, 150 mM NaCl, 2 mM $MgCl_2$, 1 mM DTT, 0.1 mM EDTA, 10% glycerol, 100 U/ml RNase inhibitor, and 1× protease inhibitor cocktail [Roche]). The lysate was precleared by centrifugation, and the supernatant was incubated with anti-CSL antibodies (Cell Signaling) or nonimmune IgGs overnight at 4°C. RNA-protein complexes were captured with antibody-coupled protein A magnetic beads, washed with RIP buffer, and treated with RNase-free DNase I. RNAs were isolated using the Trizol method. Approximately 200 ng of RNA from both immunoprecipitation and mock (nonimmune IgG) pull-down was converted to cDNA using random hexamer primer. The RT-qPCR was carried out with lncRNA-specific primers, and fold enrichment was calculated against mock.

Tumorigenesis experiments. Mouse intradermal tumorigenicity ear injection assays were carried out in 8- to 10-week-old female NOD.Cg-Prkdcscid Il2rgtm1Wjl/SzJ mice (The Jackson Laboratory), as in ref. 5. Assays were conducted with the indicated combinations of cells: EGFP-expressing SCC13 cells (1×10^5), EGFP-expressing CAL27 cells (1×10^5), FUCCI-expressing SK-MEL-23 cells (1×10^5), or SK-MEL-28 cells expressing dsRed (1×10^5) were admixed with equal numbers of HDFs with or without shRNA-mediated silencing of AR or with CAFs with or without AR overexpression. Cells were injected 5 μl per site using a 33-gauge microsyringe (Hamilton).

Data and software availability. Data sets generated for this study were deposited in the NCBI Gene Expression Omnibus (GEO) public repository (GSE107319, "Androgen receptor functions as transcriptional repressor of Cancer Associated Fibroblast (CAF) activation [RNA-seq]").

Statistics. Data are presented as mean ± SEM or mean ± SD, as indicated in the legends. For qPCR gene expression assays, histograms represent the value of each single strain. For gene expression and functional testing assays, statistical significance of differences between experimental groups and controls was assessed by 2-tailed unpaired or paired *t* test or by 1-way ANOVA with Dunnett's test to correct for multiple comparisons, as indicated in the figure legends. A P value less than 0.05 was considered as statistically significant. For each experiment, at least 3 separate HDF strains were used in the independent experiments. For ChIP–re-ChIP experiments, because of the complexity of the setting, the experiment was carried out in 1 strain. For ChIP assay regarding the AR histone modifications of AR promoter, 2 strains were used.

For ear injection/tumorigenicity assays, the individual animal variability issue was minimized by contralateral ear injections of the same animals with control versus experimental combinations of cells. No statistical method was used to predetermine sample size in animal experiments. No exclusion criteria were adopted for studies and sample collection. No randomization was used, and the researchers were not blinded.

Study approval. HDFs were prepared from discarded human skin samples from abdominoplasty or circumcision at the Department of Surgery or Pediatrics, Lausanne University, with required institutional approvals (UNIL: CER-VD 222/12) and informed consent. Matched normal human skin samples and samples of SCCs were obtained at the Department of Dermatology, Massachusetts General Hospital, as discarded parts not needed for diagnosis. All samples were processed as approved by the institutional review board (MGH: 2000P002418) and as described in refs. 5, 33. Matched normal skin and AK sections were provided by the Department of Dermatology, University of Tubingen, with institutional review board approvals and informed consent, as previously reported in ref. 5. Dysplastic nevus skin sections were obtained from the Department of Dermatology, University Hospital Zürich, with institutional review board approvals and informed consent. Experiments on human-derived material followed the principles of the Declaration of Helsinki as well as the Swiss laws governing human research.

All samples were obtained as surplus material from consenting patients (Ek.647/800), and the experiments were approved by the Kantonal ethical committee of Zürich (Kantonale Ethikkommission Zürich, Zürich, Switzerland, approval no. KEK.Zh.Nr. 2014-0425). No access to sensitive information has been provided. Animal studies were approved by the Massachusetts General Hospital Institutional Animal Care and Use Committee (MGH: 2004N000170).

Sample size and reproducibility of the experiments. Sample size and replication of the experiment were evaluated using 3 or more independent strains of HDFs or skin-derived CAFs as stated in the figure legends. Independent infections of lentiviral vectors for gene silencing with shRNA lentiviral vectors were used. In vivo experiments were carried out using independent strains of HDFs or CAFs with corresponding genetic manipulations. Each ear injection experiment used an independent strain of HDFs.

See Supplemental Methods online for additional methods.

Author contributions

AC, SG, MGP, LM, SG, PB, GB, AK, and BCÖ performed the experiments and/or contributed to analysis of the results. PO performed the bioinformatics analysis. ML, PK, RD, and VN provided clinical samples. AC, SG, and GPD designed the study and wrote the manuscript.

Acknowledgments

We thank Karl-Henning Kalland for the gift of AR-expressing lentiviral vector. AC was supported by an AIRC–Marie Curie fellowship from the Italian Association for Cancer Research and the European Union FP7 Marie Curie Program. This work was supported by grants from the NIH (R01AR039190, R01AR064786; the content does not necessarily represent the official views of the NIH), the Swiss National Science Foundation (310030B_176404, "Genomic instability and evolution in cancer stromal cells"), and the European Research Council (26075083) to GPD.

Address correspondence to: G. Paolo Dotto, Department of Biochemistry, University of Lausanne, Chemin des Boveresses 155, Epalinges 1066, Switzerland. Phone: 41.21.692.57.20; Email: paolo.dotto@unil.ch.

1. Campisi J, Andersen JK, Kapahi P, Melov S. Cellular senescence: a link between cancer and age-related degenerative disease? *Semin Cancer Biol*. 2011;21(6):354–359.
2. Kalluri R. The biology and function of fibroblasts in cancer. *Nat Rev Cancer*. 2016;16(9):582–598.
3. Junttila MR, de Sauvage FJ. Influence of tumour micro-environment heterogeneity on therapeutic response. *Nature*. 2013;501(7467):346–354.
4. Polanska UM, Orimo A. Carcinoma-associated fibroblasts: non-neoplastic tumour-promoting mesenchymal cells. *J Cell Physiol*. 2013;228(8):1651–1657.
5. Procopio MG, et al. Combined CSL and p53 downregulation promotes cancer-associated fibroblast activation. *Nat Cell Biol*. 2015;17(9):1193–1204.
6. Kim DE, et al. Convergent roles of ATF3 and CSL in chromatin control of cancer-associated fibroblast activation. *J Exp Med*. 2017;214(8):2349–2368.
7. Clocchiatti A, Cora E, Zhang Y, Dotto GP. Sexual dimorphism in cancer. *Nat Rev Cancer*. 2016;16(5):330–339.
8. Klein SL, Flanagan KL. Sex differences in immune responses. *Nat Rev Immunol*. 2016;16(10):626–638.
9. Yoshida S, et al. Androgen receptor promotes sex-independent angiogenesis in response to ischemia and is required for activation of vascular endothelial growth factor receptor signaling. *Circulation*. 2013;128(1):60–71.
10. Ashcroft GS, Mills SJ. Androgen receptor-mediated inhibition of cutaneous wound healing. *J Clin Invest*. 2002;110(5):615–624.
11. Lai JJ, et al. Monocyte/macrophage androgen receptor suppresses cutaneous wound healing in mice by enhancing local TNF-α expression. *J Clin Invest*. 2009;119(12):3739–3751.
12. Celec P, Ostatníková D, Hodosy J. On the effects of testosterone on brain behavioral functions. *Front Neurosci*. 2015;9:12.
13. Snaterse G, Visser JA, Arlt W, Hofland J. Circulating steroid hormone variations throughout different stages of prostate cancer. *Endocr Relat Cancer*. 2017;24(11):R403–R420.
14. Kono M, Fujii T, Lim B, Karuturi MS, Tripathy D, Ueno NT. Androgen receptor function and androgen receptor-targeted therapies in breast cancer: a review. *JAMA Oncol*. 2017;3(9):1266–1273.
15. Matsumoto T, et al. The androgen receptor in health and disease. *Annu Rev Physiol*. 2013;75:201–224.
16. Cioni B, et al. Loss of androgen receptor signaling in prostate cancer-associated fibroblasts (CAFs) promotes CCL2- and CXCL8-mediated cancer cell migration. *Mol Oncol*. 2018;12(8):1308–1323.
17. Lai JJ, Lai KP, Zeng W, Chuang KH, Altuwaijri S, Chang C. Androgen receptor influences on body defense system via modulation of innate and adaptive immune systems: lessons from conditional AR knockout mice. *Am J Pathol*. 2012;181(5):1504–1512.
18. Leach DA, et al. Stromal androgen receptor regulates the composition of the microenvironment to influence prostate cancer outcome. *Oncotarget*. 2015;6(18):16135–16150.
19. Liao CP, et al. Androgen receptor in cancer-associated fibroblasts influences stemness in cancer cells. *Endocr Relat Cancer*. 2017;24(4):157–170.
20. Nash C, Boufaied N, Mills IG, Franco OE, Hayward SW, Thomson AA. Genome-wide analysis of AR binding and comparison with transcript expression in primary human fetal prostate fibroblasts and cancer associated fibroblasts. *Mol Cell Endocrinol*. 2018;471:1–14.
21. Lai KP, Yamashita S, Huang CK, Yeh S, Chang C. Loss of stromal androgen receptor leads to suppressed prostate tumourigenesis via modulation of pro-inflammatory cytokines/chemokines. *EMBO Mol Med*. 2012;4(8):791–807.
22. Kopan R, Ilagan MX. The canonical Notch signaling pathway: unfolding the activation mechanism. *Cell*. 2009;137(2):216–233.
23. Heemers HV, Tindall DJ. Androgen receptor (AR) coregulators: a diversity of functions converging on and regulating the AR transcriptional complex. *Endocr Rev*. 2007;28(7):778–808.
24. Tarulli GA, Butler LM, Tilley WD, Hickey TE. Bringing androgens up a NOTCH in breast cancer. *Endocr Relat Cancer*. 2014;21(4):T183–T202.
25. Shain AH, Bastian BC. From melanocytes to melanomas. *Nat Rev Cancer*. 2016;16(6):345–358.
26. Helsen C, et al. Androgen receptor antagonists for prostate cancer therapy. *Endocr Relat Cancer*. 2014;21(4):T105–T118.
27. Bar J, Moskovits N, Oren M. Involvement of stromal p53 in tumor-stroma interactions. *Semin Cell Dev Biol*. 2010;21(1):47–54.
28. Sakaue-Sawano A, et al. Visualizing spatiotemporal dynamics of multicellular cell-cycle progression. *Cell*. 2008;132(3):487–498.
29. Subramanian A, et al. Gene set enrichment analysis: a knowledge-based approach for interpreting genome-wide expression profiles. *Proc Natl Acad Sci U S A*. 2005;102(43):15545–15550.
30. Ghosh SK, Patton JR, Spanjaard RA. A small RNA derived from RNA coactivator SRA blocks steroid receptor signaling via inhibition of Pus1p-mediated pseudouridylation of SRA: evidence of a novel RNA binding domain in the N-terminus of steroid receptors. *Biochemistry*. 2012;51(41):8163–8172.
31. Zhang A, et al. LncRNA HOTAIR enhances the androgen-receptor-mediated transcriptional program and drives castration-resistant prostate cancer. *Cell Rep*. 2015;13(1):209–221.
32. Filippakopoulos P, Knapp S. Targeting bromodomains: epigenetic readers of lysine acetylation. *Nat Rev Drug Discov*. 2014;13(5):337–356.
33. Goruppi S, Procopio MG, Jo S, Clocchiatti A, Neel V, Dotto GP. The ULK3 kinase is critical for convergent control of cancer-associated fibroblast activation by CSL and GLI. *Cell Rep*. 2017;20(10):2468–2479.
34. Stanworth RD, Jones TH. Testosterone for the aging male; current evidence and recommended

practice. *Clin Interv Aging*. 2008;3(1):25–44.
35. Mauvais-Jarvis F. Estrogen and androgen receptors: regulators of fuel homeostasis and emerging targets for diabetes and obesity. *Trends Endocrinol Metab*. 2011;22(1):24–33.
36. Hendriksen PJ, et al. Evolution of the androgen receptor pathway during progression of prostate cancer. *Cancer Res*. 2006;66(10):5012–5020.
37. Chen WY, et al. Loss of SPDEF and gain of TGFBI activity after androgen deprivation therapy promote EMT and bone metastasis of prostate cancer. *Sci Signal*. 2017;10(492):eaam6826.
38. Pu Y, et al. Androgen receptor antagonists compromise T cell response against prostate cancer leading to early tumor relapse. *Sci Transl Med*. 2016;8(333):333ra47.
39. Li WQ, et al. Personal history of prostate cancer and increased risk of incident melanoma in the United States. *J Clin Oncol*. 2013;31(35):4394–4399.
40. Thomsen FB, et al. Risk of malignant melanoma in men with prostate cancer: nationwide, population-based cohort study. *Int J Cancer*. 2016;138(9):2154–2160.
41. Desautels D, Czaykowski P, Nugent Z, Demers AA, Mahmud SM, Singh H. Risk of colorectal cancer after the diagnosis of prostate cancer: a population-based study. *Cancer*. 2016;122(8):1254–1260.
42. Gillessen S, Templeton A, Marra G, Kuo YF, Valtorta E, Shahinian VB. Risk of colorectal cancer in men on long-term androgen deprivation therapy for prostate cancer. *J Natl Cancer Inst*. 2010;102(23):1760–1770.
43. Sharp A, Welti J, Blagg J, de Bono JS. Targeting androgen receptor aberrations in castration-resistant prostate cancer. *Clin Cancer Res*. 2016;22(17):4280–4282.
44. Watson PA, Arora VK, Sawyers CL. Emerging mechanisms of resistance to androgen receptor inhibitors in prostate cancer. *Nat Rev Cancer*. 2015;15(12):701–711.
45. Restivo G, et al. IRF6 is a mediator of Notch pro-differentiation and tumour suppressive function in keratinocytes. *EMBO J*. 2011;30(22):4571–4585.
46. Brooks YS, et al. Multifactorial ERβ and NOTCH1 control of squamous differentiation and cancer. *J Clin Invest*. 2014;124(5):2260–2276.
47. Schmidl C, Rendeiro AF, Sheffield NC, Bock C. ChIPmentation: fast, robust, low-input ChIP-seq for histones and transcription factors. *Nat Methods*. 2015;12(10):963–965.
48. Zhao J, et al. Genome-wide identification of polycomb-associated RNAs by RIP-seq. *Mol Cell*. 2010;40(6):939–953.